
Methods¹

Expedition 334 Scientists²

Chapter contents

Introduction, operations, and curation	1
Lithostratigraphy and petrology	4
Paleontology and biostratigraphy	7
Structural geology	9
Geochemistry and microbiology	11
Physical properties	16
Paleomagnetism	23
Downhole logging	25
References	28
Figures	32
Tables	49

Introduction, operations, and curation

Information assembled in this chapter will help the reader understand the basis for shipboard observations and preliminary conclusions of Integrated Ocean Drilling Program (IODP) Expedition 334. It will also enable the interested investigator to identify data and select samples for further analysis. Information presented here concerns only shipboard operations and analyses described in the site chapters (Sites U1378–U1381). This introductory section provides an overview of shipboard operations, curatorial conventions, and general core handling and analysis. Methods used by various investigators for shore-based analyses of Expedition 334 samples and data will be described in individual publications in various professional journals and the “**Expedition research results**” chapters of this *Proceedings* volume.

Site locations

At all Expedition 334 sites, GPS coordinates from precruise site surveys were used to position the vessel on site. The only seismic system used during the cruise was the Syquest Bathymetry 2010 CHIRP subbottom profiler, which was monitored on the approach to each site to ascertain that the seafloor depth agreed with that from the precruise survey. Once the vessel was positioned at a site, the thrusters were lowered and a positioning beacon was dropped to the seafloor. The dynamic positioning control of the vessel uses navigational input from the GPS and triangulation to the seafloor beacon, weighted by the estimated positional accuracy. The final hole position was the mean position calculated from the GPS data collected over the time that the hole was occupied.

Coring and drilling operations

The advanced piston corer (APC), extended core barrel (XCB), and rotary core barrel (RCB) systems were used during Expedition 334. These standard coring systems and their characteristics are summarized in Graber et al. (2002). The APC system cuts soft sediment cores with minimal coring disturbance relative to other IODP coring systems. After the APC core barrel is lowered through the drill pipe and lands near the bit, the drill pipe is pressured up until the two shear pins that hold the inner barrel attached to the outer barrel fail. The inner barrel then advances into the formation and cuts the core. The driller can detect a successful cut, or “full stroke,” from the pressure gauge on the rig floor. The XCB

¹Expedition 334 Scientists, 2012. Methods. In Vannucchi, P., Ujiie, K., Stroncik, N., Malinverno, A., and the Expedition 334 Scientists, *Proc. IODP, 334*: Tokyo (Integrated Ocean Drilling Program Management International, Inc.).
doi:10.2204/iodp.proc.334.102.2012
²Expedition 334 Scientists’ addresses.



system is deployed when the formation becomes too stiff or too hard for the APC system. The XCB cutting shoe (bit) extends as far as ~30.5 cm ahead of the main bit in soft sediments but retracts into the main bit if hard formations are encountered.

APC refusal is conventionally defined in two ways: (1) the piston fails to achieve a complete stroke (as determined from the pump pressure reading) because the formation is too hard or (2) excessive force (>60,000 lb; ~267 kN) is required to pull the core barrel out of the formation. When full or partial stroke can be achieved but excessive force cannot retrieve the barrel, the core barrel can be “drilled over”; after the inner core barrel is successfully shot into the formation, the drill bit is advanced to total depth to free the APC barrel. This strategy allows a hole to be advanced much farther with the APC, the preferred coring tool. Nonmagnetic core barrels are commonly used during all conventional APC coring, but the APC drillover technique is not typically conducted in the first hole at each site if hard rock might be encountered. Standard steel core barrels are usually used when utilizing the drillover technique because they are stronger than the nonmagnetic barrels. Most APC/XCB cored intervals are ~9.5 m long, which is the length of a standard core barrel. However, the amount of advance during coring varied case by case. Core operations and recovery information is shown in the “Operations” section of each site chapter.

Some APC cores were oriented using the Flexit tool (see “[Paleomagnetism](#)”). Formation temperature measurements were made in Hole U1378B, Hole U1379C, and Hole U1381B (see “[Downhole logging](#)”). Downhole logging was executed in Holes U1378A and U1379A using logging while drilling (LWD).

The XCB system was used to advance the hole when APC refusal occurred in a hole before the target depth was reached and when the formation became too stiff for the APC system or when drilling hard substrate. The XCB is a rotary system with a small cutting shoe extending below the large rotary drill bit. The smaller bit can cut a semi-indurated core with less torque and fluid circulation than the main bit and thus optimizes recovery.

The bottom-hole assembly (BHA) is the lowermost part of the drill string. The exact configuration of the BHA is reported in “Operations” in each site chapter. A typical APC/XCB BHA consists of a drill bit (11⁷/₁₆ inch outer diameter), a bit sub, a seal bore drill collar, a landing saver sub, a modified top sub, a modified head sub, a nonmagnetic drill collar (for APC/XCB), a number of 8 inch (~20.32 cm) drill collars, a ta-

pered drill collar, six joints (two stands) of 5½ inch (~13.97 cm) drill pipe, and one crossover sub.

The RCB system was deployed to drill the sediment and basalt at Site U1381 because the basalt was the main target at this site. The RCB is a conventional rotary drilling system and requires a dedicated RCB BHA and a dedicated RCB drilling bit (9⁷/₈ inch outer diameter). A typical BHA for RCB coring includes an RCB drill bit, a mechanical bit release (MBR), a modified head sub, an outer core barrel, a modified top sub, and a series of drill collars followed by tapered drill collar and 5½ inch drill pipe.

Curatorial procedures and sample depth calculations

Numbering of sites, holes, cores, and samples followed standard IODP procedure. Drilling sites are numbered consecutively from the first site drilled by the *Glomar Challenger* in 1968. IODP Expedition 301 began using the prefix “U” to designate sites occupied by the US Implementing Organization (USIO) vessel, the R/V *JOIDES Resolution*. For all IODP drill sites, a letter suffix distinguishes each hole cored at the same site. The first hole cored is assigned the site number modified by the suffix “A,” the second hole takes the site number and the suffix “B,” and so forth. For Expedition 334, each site has two or more cored holes (A, B, C, etc.).

A full curatorial identifier for a sample consists of the following information: expedition, site, hole, core number, core type, section number, and interval in centimeters measured from the top of the core section and also the sampling tools and volumes taken. For example, in sediment, a sample identification of “334-U1378B-1H-2, 10–12 cm” represents a sample taken from the interval between 10 and 12 cm below the top of Section 2 of Core 1 (“H” designates that this core was taken with the APC system) of Hole B of Site U1378 during Expedition 334. For hard rocks, a sample identification of “334-U1381A-3R-8 (Piece 1, 4–7 cm)” indicates a 3 cm sample of Piece 1 removed from the interval between 4 and 7 cm below the top of Section 8 of Core 3 (“R” designates that this core was taken with the RCB) in Hole A at Site U1381. For cores taken with the XCB, the core type is indicated by an “X” after the core number. During Expedition 334, Site U1380 sediment was drilled without coring because the target recovery was underlying basement rock. Drilled intervals are assigned double-digit numbers, and the cores recovered after a drilled interval are assigned the following number in combination with the corresponding letter for drilling/coring system. For example, the drilled interval in Hole U1381A was designated 334-

U1381A-11, where the first “1” indicates drilled interval 1 and the second “1” indicates the first section of that interval that was drilled. The first core recovered in Hole U1381A after the drilled interval was designated 334-U1381A-2R (“R” for rotary core barrel).

The cored interval is measured in meters below seafloor (mbsf) according to the core depth below seafloor, method A (CSF-A), depth scale (see IODP Depth Scale Terminology at www.iodp.org/program-policies/). In general, the depth below seafloor is determined by subtracting the water depth estimated from the initial drill pipe measurement to the seafloor from the total drill pipe measurement. The depth interval assigned to an individual core begins with the depth below seafloor at which coring began and extends to the depth that coring advanced. Each coring interval is generally ~9.5 m, which is the length of a core barrel; however, coring intervals may be shorter.

During Expedition 334, unless otherwise noted, all core depths below seafloor have been calculated as CSF-A and all LWD depths calculated as LWD depth below seafloor (LSF). For ease of communication of shipboard results, all depths are reported in this volume as “mbsf” unless otherwise noted.

Core handling and analysis

As soon as cores arrived on deck, they were extracted from the core barrel in plastic liners. These liners were carried from the rig floor to the core processing area on the catwalk outside the Core Laboratory, where they were split into ~1.5 m sections. Liner caps (blue = top, colorless = bottom) were placed onto liner sections on the catwalk by the curator. Hard rock pieces were pushed to the top of the liner sections and total rock length was measured. The length was entered into the database using the SampleMaster application as “created” length. Created length is used to calculate recovery. Headspace samples were taken from freshly exposed end of a top core section and next to the interstitial water sample immediately after core retrieval using a brass boring tool or plastic syringe for immediate hydrocarbon analysis as part of the shipboard safety and pollution prevention program (see [“Geochemistry and microbiology”](#)). Typically this procedure is done in the first hole drilled at a site. However, the Environmental Protection and Safety Panel and the Texas A&M University Safety Panel approved our proposal to first drill a logging dedicated hole at Sites U1378 and U1379 using LWD techniques. This procedure was considered safe, as methane wasn’t expected to be a problem at the sites drilled during Expedition 334

and borehole pressure was constantly monitored during the LWD operation (see [“Downhole logging”](#) for detailed information on the LWD operation).

The first core from each hole (i.e., Core 1H) was sampled for bottom water if a mudline was recovered and seawater was present inside the top of the core liner (see “Operations” in each site chapter). The bottom seawater was used for comparative studies of microbial communities between seawater and subsurface habitats.

Cores from subsequent holes were processed on the catwalk, and whole-round sections were routinely taken and transferred immediately to the Geochemistry Laboratory for a wide range of geochemical and microbiological subsampling, including interstitial water extraction (see [“Geochemistry and microbiology”](#)). Once the subsampling was completed, the remaining pieces of the whole-round core sections were brought back to the Core Laboratory for routine core processing.

Basalt cores were brought to the Core Laboratory for routine core processing. After splitting, the cores were visually examined and described in detail by the shipboard petrologists and structural geologists. Subsequent to this, the scientists interested in this material for diverse geochemical and petrological studies were able to mark their samples, and, after approval by the Sample Allocation Committee, the curator proceeded to cut the samples.

As described in [“Lithostratigraphy and petrology,”](#) [“Physical properties,”](#) and [“Paleomagnetism,”](#) routine core processing in the Core Laboratory included whole-round logging of core sections and splitting into working and archive halves. Archive-half sections were then imaged with the Section Half Image Logger (SHIL), logged with the Section Half Multisensor Logger (SHMSL), and visually described for lithologic and petrological properties. The working halves were sampled for shipboard analyses and personal postexpedition research.

In the Core Laboratory, whole-round sections were split lengthwise in the core splitting room to expose the core. For hard rock cores, oriented pieces of core were marked on the bottom with a blue wax pencil to preserve orientation, either before they were extracted from the core barrel or when they were removed from the split core liner. In some cases, pieces were too small to be oriented with certainty. Adjacent but broken core pieces that could be fit together along fractures were curated as single pieces. The petrologist on shift confirmed piece matches, corrected any errors, and marked the split line on the pieces, which defined how the pieces were cut in two equal

halves. The aim was to maximize the expression of dipping structures on the cut face of the core while maintaining representative features in both archive and working halves. A plastic spacer was secured to the split core liner with acetone between individual pieces or reconstructed contiguous groups of sub-pieces. These spacers may represent a substantial interval of no recovery. The length of each section of core, including spacers, was entered into the curation database as “curated” length. Curated length commonly differs by a few to several centimeters from the created length measured on the catwalk. The database recalculates the assumed depth of each piece based on the curated length.

Core description as well as sampling for shipboard analyses and personal research was done onboard. After completing the description of the archive half and sampling of the working half, both halves of the core were then shrink-wrapped, put into labeled plastic tubes, sealed, and transferred to cold storage space aboard the ship. At the end of the expedition, the cores and samples were transferred from the ship to refrigerated containers and shipped to cold storage at the IODP Gulf Coast Repository in College Station, Texas (USA).

Drilling-induced core deformation

Cores may be significantly disturbed and contain extraneous material as a result of the coring and core handling process. Therefore, the top 10–50 cm of each core must be carefully examined for potential “fall-in” during description. Common coring-induced deformation includes concave-downward appearance of originally horizontal bedding. In APC cores, the motion of the piston may result in fluidization (flow-in) at the bottom of the cores. Retrieval from depth to the surface may result in elastic rebound. Observed core disturbances are described in the “Lithostratigraphy” section in each site chapter and graphically indicated on the core summary graphic reports (barrel sheets).

Authorship of site chapters

The separate sections of the site chapters and methods chapter were written by the following shipboard scientists (authors are listed in alphabetical order; no seniority is implied):

Operations: S. Midgley, N.A. Stroncik
 Background and objectives: K. Ujiie, P. Vannucchi
 Lithostratigraphy and petrology: I. Arroyo,
 J. Kameda, S. Kutterolf, G. MacCay, P. Sak,
 M. Stipp, M. Uno
 Paleontology and biostratigraphy: S. Foley,
 K. Ohkushi

Structural geology: G. Huftile, M. Stipp,
 A. Tsutsumi, Y. Yamamoto

Geochemistry and microbiology: M. Formolo,
 A. Martino, M. Nuzzo, E. Solomon, M. Torres

Physical Properties: U. Barkhausen, M. Conin,
 R. Harris, A. Heurret, G.Y. Kim, S. Saito,
 Y. Vadakkeyakath, J. Zhu

Paleomagnetism: Y. Usui, X. Zhao

Downhole measurements: A. Malinverno, S. Saito

Lithostratigraphy and petrology

This section outlines the procedures used to document the composition, texture, and sedimentary structure of geologic materials recovered during Expedition 334. These procedures included visual core description, smear slide and petrographic thin section description, digital color imaging, color spectrophotometry, and X-ray diffraction (XRD). Because many of the geologic techniques and observations used to analyze sedimentary cores are similar to those used to analyze igneous cores, the methods are presented together. However, as conditions warranted, different procedures were used to characterize sedimentary and crystalline basement rocks. In instances where the description protocols differ, both are described in detail.

All data were uploaded into the IODP-USIO Laboratory Information Management System (LIMS), and observations were entered using the DESClogik application in Tabular Data Capture mode. Additional details are provided below. A glossary of common geological terms used to describe the basement cores can be found in Table T1.

Core sections available for sedimentary, petrographic, and structural observation and interpretation included both the working and archive halves. Sections dominated by soft sediment were split using a thin wire held in high tension. Pieces of hard rock were split with a diamond-impregnated saw such that important compositional and structural features were preserved in both the archive and working halves. The split surface of the archive half was then assessed for quality (e.g., smearing or surface unevenness) and, if necessary, scraped lightly with a glass slide or spatula. After splitting, the archive half was imaged by the SHIL and then analyzed for color reflectance and magnetic susceptibility using the SHMSL (see “[Physical properties](#)”). In rare instances, the archive-half was reimaged when visibility of sedimentary structures or fabrics improved following treatment of the split core surface.

Following imaging, the archive sections of the sediment core were macroscopically described for litho-

logic, sedimentary, and structural features. Lithostratigraphic units were characterized by visual inspection, and smear slide samples were used to determine microfossil and sedimentary constituents and abundances to aid in lithologic classification. Cores from the basement were also described visually and subsequently with the aid of thin sections for primary and secondary igneous features. All descriptive data were entered into DESClogik using the data capture software. Based on preliminary visual descriptions and physical properties data, thin section samples and samples for XRD were extracted from the working half. All descriptions and sample locations were recorded using curated depths and then recorded on standard graphic report forms (barrel sheets) and documented on visual core description (VCD) graphic reports (Fig. F1).

Visual core descriptions for sediment

Color and composition

Color was determined qualitatively for core intervals using Munsell Color Charts (Munsell Color Company, Inc., 2000). Visual inspections of the archive halves were used to identify compositional elements of the sediment, including concretions, nodules, chert, and tephra.

To emphasize differences in the composition of volcanic sandstones, the rocks were classified using a scheme developed by Fisher and Schmincke (1984). In general, coarser grained sedimentary rocks (63 μm to 2 mm average grain size) are designated as “sand(stone),” where the volcanoclastic components were <25% of the total clast content the sample is termed a volcanoclastic rock. Volcanoclastics can be both (1) reworked and commonly altered heterogeneous volcanic material like lava, tuff, and tephra and (2) fresh, or less altered, compositionally homogeneous loose pyroclastic material resulting directly from explosive eruptions on land or effusive/explosive vents on the seafloor.

If there are $\geq 25\%$ volcanoclasts but <25% pyroclasts in the sediment/sedimentary rock, it is designated as a “volcanoclastic sand(stone).” If the clast composition is 25%–75% pyroclasts, the sediment/sedimentary rock is classified as “tuffaceous sand(stone),” but if clast composition is $\geq 75\%$ pyroclasts, the rock/sediment is classified as a “tuff” or “ash.” Depending on grain size and degree of compaction, the nomenclature is adjusted accordingly, as shown in Table T2.

Textures, structures, and sedimentary fabric

When visible at low magnification, sediment grain size was determined using the Wentworth scale (Wentworth, 1922). Grain size, particle shape, and sorting

were also noted; however, these textural attributes required inspection at high magnification and were only described on smear slides and thin sections (see below).

Sedimentary structures observed in recovered cores included bedding, soft-sediment deformation, bioturbation, and early diagenetic mineral formation. Bed thickness was defined according to Boggs (2006) and included the following units:

- Very thick bedded = >100 cm.
- Thick bedded = 30–100 cm.
- Medium bedded = 10–30 cm.
- Thin bedded = 3–10 cm.
- Very thin bedded = 1–3 cm.
- Laminae = <1 cm.

Some samples were inspected with a 10 \times hand lens for micrograded bedding (i.e., graded bedding occurring within laminations) and indications of preferred particle orientation, including lineation and imbrication of elongated detrital and biogenic material.

The abundance of bioturbation is constrained using the semiquantitative ichnofabric index as described by Droser and Bottjer (1986, 1991) and the thickness. The indexes refer to the degree of biogenic disruption of primary fabric, such as lamination, and range from 1 for nonbioturbated sediment to 6 for total homogenization:

- 1 = no bioturbation recorded; all original sedimentary structures preserved.
- 2 = discrete, isolated trace fossils; up to 10% of original bedding disturbed.
- 3 = approximately 10%–40% of original bedding disturbed. Burrows are generally isolated, but locally overlap.
- 4 = last vestiges of bedding discernible; approximately 40%–60% disturbed. Burrows overlap and are not always well defined.
- 5 = bedding is completely disturbed, but burrows are still discrete in places and the fabric is not mixed.
- 6 = bedding is nearly or totally homogenized.

The ichnofabric index in cores was identified with the help of visual comparative charts (Heard and Pickering, 2008). Distinct burrows that could be assigned to specific ichnotaxa were also recorded.

Smear slides and thin sections

Smear slides and thin sections are useful for identifying and reporting basic textural and compositional attributes, even if the results are only semiquantitative. We estimated the texture of the sediments with the help of a visual comparison chart (Rothwell, 1989). However, errors can be large, especially for the fine silt- and clay-size fractions. Smear slide analysis

also tends to underestimate the amount of sand-size grains because sand-sized particles are difficult to incorporate evenly onto the slide. Nevertheless, in order to define unit boundaries and subunits, smear slides are a fast and efficient way to evaluate differences in lithology, texture, and composition, as constrained by point counting.

Point counts were conducted in four defined areas at 100×–200× magnification. This method works well for sandstones and sandy siltstones, and the theoretical 2σ error for a total of 200 counted particles is between 3% and 7%, depending on the portion of the total inventory (van der Plas and Tobi, 1965). The various components were then binned into several categories (e.g., feldspar, pyroxene, sedimentary lithics, etc.) to facilitate optimum reproducibility among different scientists.

For fine sediments (silt and silty claystones), rough estimations were made regarding the matrix using the visual comparison chart of Rothwell (1989). These estimates were supplemented with point counting of the coarser fraction. The coarse and fine fractions were subsequently combined and normalized to 100% of the total component inventory. Because most of the point counting is based on estimates, the 2σ error for the finer sediments is much higher and must be considered when interpreting the results; the overall trends, especially for the coarser grains, are considered more reliable. We normalized the data for the finer grained sediments against three principal classes. For example, quartz or feldspar, as well as volcanoclastic or sedimentary lithic content, were normalized to total mineral and total lithic contents, respectively. Additionally, the inventory of tephra layers, pods, and dispersed ash layers was documented separately to account for the presence of glass shard textures and mineral composition. This method cannot be applied to tuffs because many fine glass shards are destroyed during smear slide preparation.

Results are summarized in the smear slides (see “[Core descriptions](#)”). The relative abundance of major components was also validated by XRD (see “[X-ray diffraction](#)”), and the absolute weight percent of carbonate was verified by chemical analysis (see “[Geochemistry and microbiology](#)”).

The sample location of each smear slide was entered into the DESClogik system with a sample code of “SS,” using the Samples application. The position of each specimen is shown on the VCD slide editor column of the VCD application.

X-ray diffraction

We completed routine XRD analyses of bulk powders using a Bruker D-4 Endeavor diffractometer mounted

with a Vantec-1 detector using nickel filtered $\text{CuK}\alpha$ radiation. Our principal objective was to determine the mineral phases present using identified peaks. Most of the samples were selected from intervals adjacent to whole-round samples, and most are part of sampling clusters with physical properties and carbonate. A few additional samples were collected periodically from such unusual lithologies such as carbonate-cemented claystone and volcanic ash. Samples were freeze-dried, crushed with a ball mill, and mounted as random bulk powders. Standard locked coupled scan conditions were

Voltage = 40 kV,
Current = 40 mA,
Goniometer scan $2\theta = 5^\circ\text{--}70^\circ$,
Step size = 0.015° ,
Scan rate = 0.1 s/step, and
Divergence slit = 0.3 mm.

The upper and lower limits of each peak on the diffractogram were adjusted following the guidelines shown in Table T2. Calculations of relative mineral abundance used a matrix of normalization factors derived from integrated peak areas and singular value decomposition (Table T3). As described by Fisher and Underwood (1995), calibration of singular value decomposition factors depends on the analysis of known weight percent mixtures of mineral standards that are appropriate matches for natural sediments (Fig. F2).

In the final assessment, calculated values of a mineral’s weight percent should only be regarded as relative percentages within a four-component system where clay minerals + quartz + plagioclase + calcite = 100%. How close those estimates are to the absolute percentages within the mass of total solids will depend on the abundance of amorphous solids (e.g., biogenic opal and volcanic glass), as well as the total of all other minerals that occur in minor or trace quantities. For most natural samples, absolute errors are probably between 5% and 10% (Fisher and Underwood, 1995). Thus, the primary value of bulk powder XRD data should be to identify spatial and temporal trends in sediment composition and to assist with core-log integration.

Basement description

In order to preserve important features and structures, all cores were visually examined before being split. Large pieces of basement core were marked on the bottom with a red wax pencil to preserve orientation when they were removed from the split core liner. In many cases, pieces were too small to be oriented with certainty. Each piece was numbered sequentially from the top of each core section and labeled on the outside surface. Broken core pieces that

could be fit together along fractures were assigned the same number and lettered consecutively from the top down (e.g., 1A, 1B, and 1C). Plastic spacers were placed between pieces with different numbers. The presence of a spacer may represent a substantial interval without recovery. Fitted core pieces were not glued, but wrapped together into plastic foil.

Characterization of the basement is based on visual core description and thin section analyses. Morphology of magmatic contacts, veins, lava, and porphyroclastic flows were initially identified on the whole-round cores and further described and measured after splitting the cores. A hand lens (10×) and binocular microscope helped to distinguish between the different types of sedimentary and igneous rocks. Petrographic texture, grain size, and phenocryst mineralogy as well as modal abundance were determined using thin section analysis. When describing and assigning a name to a rock interval, cores were divided based on changes in mineralogy, texture, grain size, composition, the occurrence of chilled margins, or tectonic contacts.

VCD forms were used to describe each basement core. A key summarizing the symbols used on the hard rock VCDs is given in Figure F3. On the VCDs, the following information is displayed from left to right:

- Section scale from 0 to 150 cm;
- Piece number;
- Photograph of the archive half of the core;
- Piece orientation;
- Lithology symbol;
- Phenocrysts abundance, if igneous;
- Phenocrysts minerals, if igneous;
- Alteration intensity;
- Information about abundance and filling of veins;
- Description of primary and secondary magmatic structures in the rock; and
- Any additional comments.

In instances where an individual rock fragment could not have rotated about a horizontal axis during drilling, an arrow pointing toward the top of the section was inserted into the Piece orientation column. The term “vein” describes any filled, crosscutting fractures, which include breccia-filled fractures, epigenetic mineralized veins, shear veins, and vein networks. Vein geometry and mineralogy is given in detail in the Additional comments column. Comments also include accessory mineral occurrence.

Thin sections were studied to complete and refine the hand specimen observations. In the case of igneous rocks, textures were defined at the microscopic

scale according to the degree of crystallinity of the groundmass (holohyaline to holocrystalline). A visual estimate of the modal abundance of the phenocrysts was made, average crystal size for each mineral phase was determined, and the mineral shape and mineral habit were also determined using thin sections. The textural terms “euhedral,” “subhedral,” “anhedral,” and “interstitial” are used to describe the habit of crystals. Grain shape was divided into four classes:

- Equant (aspect ratio = <1:2),
- Subequant (aspect ratio = 1:2 to 1:3),
- Tabular (aspect ratio = 1:3 to 1:5), and
- Elongate (aspect ratio = >1:5).

Basalt and all other rocks exclusively occur within the cored units that have been ascribed to the transition zone between upper plate sediment and basement arcward of the trench. Here, the constituent blocks of this transition zone are clasts composed of basalt, breccia, limestone, radiolarian chert, and argillaceous matrix material. Sediments in the basement are considered to be lithics and are therefore described in the same manner as the sedimentary cover. Outboard of the trench, the predominant basement rocks are basalt, which are distinguished on the basis of matrix appearance; the presence of phenocryst minerals; alteration state; and overprinting by intrusions, faulting and veining.

All classifications together with the basement core descriptions and associated shipboard analyses were archived electronically in DESClogik. DESClogik is a VCD program that stores visual (macroscopic and/or microscopic) description information about core structures at a given section index. Figure F3 displays graphic patterns for all basement lithologies encountered during Expedition 334.

Paleontology and biostratigraphy

Paleontological investigations carried out during the expedition focused primarily on calcareous nannofossils and planktonic and benthic foraminifers. Preliminary biostratigraphic and paleontological determinations in Holes U1378B, U1379C, U1380A, and U1381A are based on calcareous nannofossil and planktonic foraminiferal datums and bioevents.

Calcareous nannofossils

Sediment sample processing

Calcareous nannofossil assemblages were examined and described using smear slides made from core catcher samples. If the core catcher sample was bar-

ren, at least one additional sample from the particular section of core was examined. A standard smear slide preparation was used for immediate biostratigraphic examination. For this process, a small portion of the raw material was placed directly onto a glass coverslip. A drop of distilled water was added, and a flat-sided toothpick was used to spread the sediment over the coverslip, which was then dried rapidly on a hot plate. With sediment-side down, the coverslip was mounted onto a glass microscope slide with Norland optical adhesive. All samples were examined by light microscopy using phase contrast, brightfield, and cross-polarized light under magnifications of 400 \times and 1000 \times .

Relative abundances were determined using the method of Hay (1970) as follows:

- H = highly abundant (>100 specimens per field of view).
- V = very abundant (11–100 specimens per field of view).
- A = abundant (1–10 specimens per field of view).
- C = common (1 specimen per 2–10 fields of view).
- F = few (1 specimen per 11–100 fields of view).
- R = rare (1 specimen per 101–1000 fields of view).

The following basic criteria were used to qualitatively provide a measure of preservation of the nanofossil assemblage:

- G = good (no dissolution or overgrowth).
- M = moderate (slight dissolution and/or overgrowth).
- P = poor (considerable dissolution and/or overgrowth).

Standard zonations by Martini (1971), Bukry (1973, 1975), and Okada and Bukry (1980) were utilized during the study to evaluate nanofossil age datums. The zonal scheme of Martini (1971) was selected for the range-distribution chart. These datums were correlated to the geomagnetically derived chronologic timescale of Berggren et al. (1995a, 1995b) for the Pleistocene and Pliocene. Although not utilized in this study, we acknowledge the June 2009 ratification of the redefinition of the base of the Pleistocene (see Ogg et al., 2008, and recent revisions), which pushes the Pliocene/Pleistocene boundary back from 1.806 to 2.588 Ma.

Foraminifers

Sediment sample processing

Core catcher samples were processed following routine methods for the study of foraminifers. Core catcher samples first were dried and weighed. Dry sediment was washed with distilled water over a 63

μm wire mesh sieve. Indurated samples were soaked in water for a short time prior to washing to promote disaggregation of the sediment. Once sieved, all samples were dried on filter paper in a low-temperature oven at $\sim 60^\circ\text{C}$, weighed, and subsequently examined under a binocular microscope. To minimize contamination of foraminifers between samples, the sieve was placed into a sonicator for several minutes and thoroughly checked between samples to enable identification of contaminants from previous samples. Species identification for planktonic foraminifers were generally made on the $>63\ \mu\text{m}$ size fractions. Planktonic and benthic foraminiferal abundance data were based on counts of ~ 50 specimens from the $>63\ \mu\text{m}$ size fractions where possible. The preservation, abundance, and zonal assignment for selected samples were entered through DESClogik before uploading into the LIMS database.

The preservation status of planktonic and benthic foraminifers was estimated as follows:

- VG = very good (no evidence of overgrowth, dissolution, or abrasion).
- G = good (little evidence of overgrowth, dissolution, or abrasion).
- M = moderate (calcite overgrowth, dissolution, or abrasion are common but minor).
- P = poor (substantial overgrowth, dissolution, or fragmentation).

Planktonic foraminiferal zonal scheme and taxonomy

The planktonic foraminifer zonal scheme used here follows Blow (1969). This scheme is widely employed in tropical regions. Incorporated into this zonation are the modifications proposed by Kennett and Srinivasan (1983). Age calibration of planktonic foraminiferal datums follows that of Wade et al. (2011).

Benthic foraminiferal taxonomy and paleodepth determination

Taxonomic assignments follow Jones (1994). The generic classification of Loeblich and Tappan (1988) was used. The depth distribution of benthic foraminifers is based on recent ecological data of Bandy and Arnal (1957), Crouch and Poag (1987), Heinz et al. (2008), and Smith (1963, 1964) reported from the Pacific off Central America.

Relative percentages of benthic to planktonic tests are also available to evaluate relative changes in paleobathymetry (Ingle et al., 1980). Relative percentages of benthic to planktonic tests were determined

by counting specimens on the picking tray during Expedition 334.

Structural geology

Our methods for documenting the structural geology of Expedition 334 cores largely followed those given by the Expeditions 315 and 316 structural geologists (Expedition 315 Scientists, 2009; Expedition 316 Scientists, 2009). We documented the deformation observed in the split cores by classifying structures, determining the depth extent, measuring orientation data, and recording kinematic information. The collected data were logged manually onto a printed form at the core table and then typed into both a spreadsheet and the DESClogik database. Where possible, the orientation data were also corrected for rotation related to drilling on the basis of paleomagnetic declination and inclination information.

Structural data acquisition and orientation measurements

Each structure was recorded manually on a description table sheet modified from that used during Expedition 316 (Fig. F4). Core measurements followed those made during Expeditions 315 and 316, which in turn were based on previous Ocean Drilling Program (ODP) procedures developed at the Nankai accretionary margin (i.e., ODP Legs 131 and 190). We used a plastic protractor for orientation measurements (Fig. F5). Using the working half of the split core provided greater flexibility in removing—and cutting, if necessary—pieces of the core for measurements.

Orientations of planar and linear features in cored materials were determined relative to the core axis, which represents the vertical axis in the core reference frame, and the “double line” marked on the working half of the split core liner, which represents 0° (and 360°) in the plane perpendicular to the core axis (Fig. F6). To determine the orientation of a planar structural element, two apparent dips of this element were measured in the core reference frame and converted to a plane represented by dip angle and either a strike or dip direction (Fig. F7). One apparent dip is usually represented by the intersection of the planar feature with the split face of the core and it is quantified by measuring the dip direction and angle in the core reference frame (in β_1 ; Fig. F8). Typical apparent dip measurements have a trend of 90° or 270° and range in plunge from 0° to 90°. The second apparent dip is usually represented by the intersection of the planar feature and a cut or fractured surface at a high angle to the split face of the core. In most cases, this was a surface either parallel or per-

pendicular to the core axis. In the former cases, the apparent dip lineation trended 000° or 180° and plunged from 0° to 90°; in the latter cases, the trend ranged from 000° to 360° and plunged 0°. Linear features observed in the cores were always associated with planar structures (e.g., striations on faults), and their orientations were determined by measuring either the rake (or pitch) on the associated plane or the trend and plunge in the core reference frame. During Expedition 334, we measured rake for striations on fault surface and azimuth and plunge for other lineation (e.g., fold axes). All data were recorded on the log sheet with appropriate depths and descriptive information.

Paleomagnetic correction

Paleomagnetic data were used during Expedition 334 to restore the structural data with respect to the geographic reference system (Fig. F7). Especially in the XCB and RCB intervals at Sites U1378–U1380, drilling-induced biscuiting of the cores and individual rotation of each core biscuit requires paleomagnetic reorientation to make the structural data usable. Given the cores taken by the APC are continuous, we can use the orientation data from discrete paleomagnetic samples or from the orientation tool attached to the APC to restore all structural data collected from the same core. In the XCB and RCB intervals, we have to take discrete samples for paleomagnetic correction because of rotation of each biscuit. We therefore recorded “coherent intervals for paleomagnetic correction” (i.e., intact and undisturbed intervals without internal biscuiting) when we identified structures. We collected paleomagnetic measurement samples from the same coherent core piece in which structures were measured. After the paleomagnetic measurements, we reoriented the structural data using the declination of the characteristic remanence of magnetization (see “Paleomagnetism”).

Description and classification of structures

We made a structural geology template for DESClogik and described and classified the structures observed. For clarity, we defined the terminology used to describe fault-related rocks, as well as the basis for differentiating natural structures from drilling-induced features.

Faults were classified into several categories based on the sense of fault slip and their structural characteristics. The sense of the fault slip was identified using offsets of markers (e.g., bedding and older faults) across the fault plane and predominantly by slickensteps. A fault with cohesiveness across the fault was described as a healed fault. Zones of dense fracture distribution and intense deformation were termed

“brecciated zones” and “fractured zones.” Here, fractured zones are moderately deformed zones with decimeter-size fragments; brecciated zones are intensively deformed zones with centimeter-size and smaller fragments, containing a few larger fragments.

In basement rocks, igneous rocks and tectonic mélanges were expected corresponding to the onshore geological map of Osa Peninsula. Whereas lithology and mineralogy of the vein minerals were described by the petrologists, orientations of the veins, foliations, and other structural features in the igneous rocks were measured by the structural geologists.

Natural structures can be strongly disturbed by drilling-induced disturbances such as flow-in structures in APC cores and biscuiting, fracturing, faulting, and rotation of fragments in XCB and RCB cores. If structures were disturbed by flow-in >60% of the cross section of the core, we excluded measurements because of the intense disturbance (bending, rotation, etc.) of these structures. To correct for the possible rotations of the fault orientation caused by coring, we used paleomagnetic data. Helicoidal striated surfaces or polished surfaces showing striations that diverge outward most likely indicated drilling-induced faults/fractures resulting from the torque exerted by the bit on the drilled material. In contrast, faults that display more planar geometry, parallel striations, and orientations compatible with multiple faults nearby (i.e., defining a system) are likely to be natural. When multiple orientation measurements were plotted in stereographic projection, natural faults were expected to display preferred orientations (i.e., strike and dip) that may be related to coherent tectonic stress orientations, whereas drilling-induced faults/fractures were expected to yield random orientation distributions.

Calculation of plane orientation

For planar structures (e.g., bedding or faults), two apparent dips on two different surfaces (e.g., one being the split core surface, which is east–west vertical, and the other being the horizontal or north–south vertical surface) were measured in the core reference frame as azimuths (measured clockwise from north, looking down) and plunges (Figs. F6, F7, F8). A coordinate system was defined in such a way that the positive x -, y -, and z -directions coincide with north, east, and vertical downward, respectively. If the azimuths and plunges of the two apparent dips are given as (α_1, β_1) and (α_2, β_2) , respectively, as in Figure F8, then the unit vectors representing these two lines, v_1 and v_2 , are

$$v_1 = \begin{pmatrix} l_1 \\ m_1 \\ n_1 \end{pmatrix} = \begin{pmatrix} \cos \alpha_1 \cos \beta_1 \\ \sin \alpha_1 \cos \beta_1 \\ \sin \beta_1 \end{pmatrix}$$

and

$$v_2 = \begin{pmatrix} l_2 \\ m_2 \\ n_2 \end{pmatrix} = \begin{pmatrix} \cos \alpha_2 \cos \beta_2 \\ \sin \alpha_2 \cos \beta_2 \\ \sin \beta_2 \end{pmatrix}.$$

The unit vector normal to the plane, v_n (Fig. F8), is then defined as

$$v_n = \begin{pmatrix} l_n \\ m_n \\ n_n \end{pmatrix} = \frac{v_1 \times v_2}{|v_1 \times v_2|},$$

where

$$v_1 \times v_2 = \begin{pmatrix} \begin{vmatrix} m_1 & m_2 \\ n_1 & n_2 \end{vmatrix} \\ \begin{vmatrix} n_1 & n_2 \\ l_1 & l_2 \end{vmatrix} \\ \begin{vmatrix} l_1 & l_2 \\ m_1 & m_2 \end{vmatrix} \end{pmatrix} = \begin{pmatrix} m_1 n_2 - m_2 n_1 \\ n_1 l_2 - n_2 l_1 \\ l_1 m_2 - l_2 m_1 \end{pmatrix}.$$

The azimuth, α_n , and plunge, β_n , of v_n are given by

$$\alpha_n = \tan^{-1} \left(\frac{m_n}{l_n} \right), \beta_n = \sin^{-1} n_n.$$

The dip direction, α_d , and dip angle, β , of this plane are α_n and $90^\circ + \beta_n$, respectively, when $\beta_n < 0^\circ$ (Fig. F9A). They are $\alpha_n \pm 180^\circ$ and $90^\circ - \beta_n$, respectively, when $\beta_n \geq 0^\circ$ (Fig. F9B). The right-hand rule strike of this plane, α_s , is then given by $\alpha_d - 90^\circ$.

Calculation of slickenline rake

For a fault with striations, the apparent rake angle of the striation, ϕ_a , was measured on the fault surface from either the 90° or 270° direction of the split-core surface trace (Figs. F7, F10). Fault orientation was measured as described above. Provided that v_n and v_c are unit vectors normal to the fault and split core surfaces, respectively, the unit vector of the intersection line, v_i , is perpendicular to both v_n and v_c (Fig. F10) and is therefore defined as

$$v_i = \begin{pmatrix} l_i \\ m_i \\ n_i \end{pmatrix} = \frac{v_n \times v_c}{|v_n \times v_c|},$$

where

$$v_c = \begin{pmatrix} 1 \\ 0 \\ 0 \end{pmatrix}$$

and

$$v_n \times v_c = \begin{pmatrix} \left| \begin{array}{cc} m_n & 0 \\ n_n & 0 \end{array} \right| \\ \left| \begin{array}{cc} n_n & 0 \\ l_n & 1 \end{array} \right| \\ \left| \begin{array}{cc} l_n & 1 \\ m_n & 0 \end{array} \right| \end{pmatrix} = \begin{pmatrix} 0 \\ n_n \\ -m_n \end{pmatrix}.$$

Knowing the right-hand rule strike of the fault plane, α_s , the unit vector, v_s , toward this direction is then

$$v_s = \begin{pmatrix} \cos \alpha_s \\ \sin \alpha_s \\ 0 \end{pmatrix}.$$

The rake angle of the intersection line, ϕ_i , measured from the strike direction is given by

$$\phi = \cos^{-1}(v_s \times v_i),$$

because

$$v_s \times v_i = |v_s||v_i|\cos\phi_i = \cos\phi_i, \therefore |v_s| = |v_i| = 1.$$

The rake angle of the striation, ϕ , from the strike direction is $\phi_i \pm \phi_a$, depending on which direction the apparent rake was measured from and which direction the fault plane dips toward. ϕ_a should be subtracted from ϕ_i when the fault plane dips toward west and ϕ_a was measured from either the top or 90° direction (Fig. F11A) or when the fault plane dips toward east and ϕ_a was measured from either the bottom or 90° direction (Fig. F11B). On the other hand, ϕ_a should be added to ϕ_i when the fault plane dips toward east and ϕ_a was measured from either the top or 270° direction (Fig. F11C) or when the fault plane dips toward west and ϕ_a was measured from either the bottom or 270° direction (Fig. F11D).

Azimuth correction using paleomagnetic data

Provided that a core is vertical, its magnetization is primary, and its bedding is horizontal, its paleomagnetic declination (α_p) indicates magnetic north when inclination (β_p) $\geq 0^\circ$ (Figs. F7, F12A), whereas α_p indicates magnetic south when $\beta_p < 0^\circ$ (Fig. F12B). The dip direction and strike of a plane in the geographic reference frame, α_d^* and α_s^* , are therefore

$$\alpha_d^* = \alpha_d - \alpha_p$$

and

$$\alpha_s^* = \alpha_s - \alpha_p$$

when

$$\beta_p \geq 0^\circ$$

and are

$$\alpha_d^* = 180^\circ + \alpha_d - \alpha_p$$

and

$$\alpha_s^* = 180^\circ + \alpha_s - \alpha_p$$

when

$$\beta_p < 0^\circ.$$

If the core was complete and continuous, one paleomagnetism sample per section (1.5 m) was deemed sufficient. If the core was discontinuous, then each part of the core that was continuous and structurally important had to contain a paleomagnetism sample. The paleomagnetism samples were taken as cubic or cylindrical samples close to the measured structures (usually within 5 cm) and from a coherent interval that included the structure. Core fragments which were so small that a spin around an axis significantly deviating from the core axis were avoided (e.g., brecciated fragments).

DESClogik structural database

The DESClogik database represents a program to store a visual (macroscopic and/or microscopic) description of core structures at a given section index. During this expedition, only the locations of structural features, raw data collected from cores, calculated orientations in the core coordinate, and restored orientation based on the paleomagnetic data were input into DESClogik, and orientation data management and planar and linear fabric analysis were done with a spreadsheet as mentioned above.

Geochemistry and microbiology

The Costa Rica Seismogenesis Project (CRISP) was designed to understand the processes that control fault zone behavior during earthquake nucleation and rupture propagation at erosional subduction zones. The first phase of this project focuses on sampling sediments, fluids, and crustal rocks to fully characterize the eroding material before subduction. Fluids

and associated diagenetic reactions are a key component of this study, as they affect hydrological parameters (e.g., permeability and pore pressure) and may regulate the mechanical state of the plate interface at depth. The concentration of dissolved species and their isotopic composition provide critical data for the identification of fluid sources, fluid-rock reactions, pathways of fluid migration, and plumbing of the system. In addition, geochemical data can help characterize the subsurface biosphere and aid in constraining mass balance inventories operating in this subduction zone. To this aim, the geochemical and microbiological sampling and analyses were coordinated so as to generate an integrated plan. Whereas the sampling frequency varies among sites (as described in each site chapter), the sampling package consisted of 5–40 cm long whole rounds for interstitial water and a 2 cm long whole round for a cluster of sediment analyses (Fig. F13). The material from the cluster sample was divided for shipboard and shore-based geochemical and physical property studies. Two routine sediment plugs were collected adjacent to each interstitial water sample for headspace analyses; one was used for standard hydrocarbon concentration monitoring on board and the other was for stable isotope measurements at onshore laboratories. Whole-round samples for microbiological studies were collected only in selected cores; these 5 cm whole rounds were cut adjacent to the interstitial water samples.

Fluid inorganic geochemistry

Interstitial water collection

For interstitial water analyses, whole-round cores were cut on the catwalk, capped, and taken to the laboratory for processing. Samples collected from 0 to 64 mbsf at Sites U1378 and from 0 to 39 mbsf at Site U1379 were processed inside a nitrogen bag to avoid oxidation of redox-sensitive elements. Whole-round samples designated for He isotopic analysis were cut on the catwalk and transferred into a plastic sealable bag initially flushed with ultrahigh purity (UHP) N₂. The sample was immediately transferred to a small processing and squeezing station set up on the upper 'tween deck of the *JOIDES Resolution*. This deck of the ship is a He-free environment, whereas the shipboard Chemistry Laboratory uses He as a carrier gas for the gas chromatographs. The sample was cleaned, squeezed, and transferred into the copper tubing in a UHP N₂ glove bag. All other cores were processed under normal atmospheric conditions. During high-resolution sampling, when there were too many interstitial water cores to process immediately, capped whole-round core sections were stored under a nitrogen atmosphere at 4°C until they were

squeezed, which occurred no later than 24 h after core retrieval.

After extrusion from the core liner, the surface of each whole-round interstitial water core sample was carefully scraped with a spatula to remove potential contamination from seawater and sediment smearing in the borehole. In APC cores, ~0.5 cm from the outer diameter, top, and bottom faces were removed, whereas in the XCB and RCB cores, where borehole contamination is higher, as much as two-thirds of the sediment was removed from each whole round. The remaining sediment (~50–300 cm³) was placed into a titanium squeezer, modified after the stainless-steel squeezer of Manheim and Sayles (1974). Gauge pressures up to 30 MPa were applied using a laboratory hydraulic press to extract interstitial water. Interstitial water was passed through a prewashed Whatman No. 1 filter fitted above a titanium screen, filtered through a 0.2 μm Gelman polysulfone disposable filter, and subsequently extruded into a pre-cleaned (10% HCl), plastic syringe attached to the bottom of the squeezer assembly. In most cases, 25–55 mL of interstitial water was collected from each sample after 20–40 min of squeezing. In the deeper sections of the sites, fluid recovery was as low as 0.5 mL after squeezing the sediment for as long as 3 h.

We undertook key biogeochemical analyses on the ship and collected appropriate interstitial water subsamples for critical categories of postcruise studies (Table T4); sample allocation was determined based on the interstitial water volume recovered and analytical priorities based on the objectives of the expedition. Because of time constraints imposed by a short expedition with high recovery and the importance of fully constraining the fluid regime at this site, we focused our efforts on collecting samples for postcruise studies and only a limited number of analyses were carried out onboard. Interstitial water subsamples were collected in glass vials for shore-based analyses of halogens, isotopic characterization of the interstitial water (oxygen and hydrogen), and dissolved metabolites (e.g., bicarbonate, sulfate, and sulfide). In addition, interstitial water subsamples were collected for analyses of dissolved volatile fatty acids, dissolved organic carbon (in glass vials and frozen), and noble gases (in copper tubing); sulfur isotope studies (fixed with 5% ZnAc); and minor and trace metal constituents and their isotopes (acidified with ultrapure nitric acid and stored in plastic vials). Shipboard analytical protocols are summarized below.

Shipboard interstitial water analyses

Salinity, alkalinity, and pH were measured immediately after squeezing, following the procedures in

Gieskes et al. (1991). Salinity was measured using a Reichert temperature-compensated handheld refractometer. pH was measured with a combination glass electrode, and alkalinity was determined by Gran titration with an autotitrator (Metrohm 794 basic Titrino) using 0.1 N HCl at 20°C. Certified reference material 104 obtained from the laboratory of Andrew Dickson, Marine Physical Laboratory, Scripps Institution of Oceanography (USA), was used for calibration of the acid. International Association for the Physical Sciences of the Oceans (IAPSO) standard seawater was used for calibration and was analyzed at the beginning and end of a set of samples for each site and after every 10 samples.

Subsamples for shore-based sulfate analysis were treated with 5 µL of 10% ZnAc per milliliter of analyte immediately after collection to precipitate ZnS. Sulfate concentrations were determined shipboard on the inductively coupled plasma-atomic emission spectrometer (ICP-AES), as detailed below, as well as with a Dionex ICS-3000 ion chromatograph, which is a reagent-free system combining automated eluent generation and self-regenerating suppression with a conductivity detector. The samples were run using a 1:100 dilution of interstitial water sample with Nanopure-grade water (18.2 MΩ). A standard curve prepared using IAPSO dilutions was run daily, and three IAPSO standards were run after every 10 samples to quantify long-term reproducibility and as quality assurance for each run.

Chloride concentrations were determined using silver nitrate (AgNO₃), as detailed by Gieskes et al. (1991).

Ammonium concentrations were determined by the indo phenol blue method using a Milton Roy Spectronic 301 spectrophotometer equipped with a Milton Roy "Mr.Sipper" sample introduction system (Gieskes et al., 1991).

Major (Ca, Mg, K, and Na) cations and sulfate concentrations were analyzed by ICP-AES with a Teledyne Prodigy high-dispersion ICP spectrometer. The general method for shipboard ICP-AES analysis of samples is described in ODP *Technical Note 29* (Murray et al., 2000) and the user manuals for new shipboard instrumentation. Samples and standards were diluted 1:200 using 2% HNO₃. Each batch of samples run on the ICP spectrometer contains blanks and solutions of known concentrations. Each item aspirated into the ICP spectrometer was counted four times from the same dilute solution within a given sample run.

Following each run of the instrument, the measured raw-intensity values were transferred to a data file and corrected for instrument drift and procedural

blank. If necessary, a drift correction was applied to each element by linear interpolation between the drift-monitoring solutions. For many of the runs there was no unidirectional instrumental drift >1% (total, through the entire run of multiple hours), and in such cases no drift correction was employed. After drift correction (where appropriate) and blank subtraction, a calibration line for each element was calculated using the results from the analyses of known solutions. The calibration lines were strongly linear and concentrations deviated only slightly from seawater concentrations. Therefore, for these elements the final concentrations were calculated on the basis of the ratio to the analysis of IAPSO seawater standard. IAPSO seawater standard was measured at least four times through a run (and as many as eight times) each time as an unknown; therefore, it was straightforward to use some IAPSO samples for precise determination of the ratio and other IAPSO samples to provide an independent check on the resultant accuracy and precision.

Fluid organic geochemistry

Routine analysis of hydrocarbon gas in sediment cores is a part of the standard IODP shipboard monitoring of the cores to ensure that the sediments being drilled do not contain greater than the expected amount of hydrocarbons. The most common method of hydrocarbon monitoring used during IODP expeditions is the analysis of gas samples obtained from either core samples (headspace analysis) or from gas expansion pockets visible through clear plastic core liners (void gas analysis), following the procedures described by Kvenvolden and McDonald (1986).

When gas pockets were detected, the free gas was drawn from the sediment void using a syringe attached to a hollow stainless-steel tool used to puncture the core liner and the void gas was analyzed on the natural gas analyzer (NGA). For headspace analyses, a 3 cm³ bulk sediment sample was collected from the freshly exposed end of a top core section and next to the interstitial water sample, immediately after core retrieval, using a brass boring tool or plastic syringe. The sediment plug was capped with a gray butyl rubber septum and sealed with an aluminum crimp cap. The vial was then heated to 70°C for ~30 min to evolve hydrocarbon gases from the sediment plug. When consolidated or lithified samples were encountered, chips of material were placed in the vial and sealed. For gas chromatographic analysis, a 5 cm³ volume of headspace gas was extracted from the sealed sample vial using a standard gas syringe and analyzed by gas chromatography.

The standard gas analysis program for safety was complemented by collecting an additional headspace sample (same resolution as described above but labeled as NZ) to measure the stable carbon and hydrogen isotope composition at onshore laboratories. The sampling method is the same as that used for the safety analysis, except that the sediment plug is extruded into a 20 cm³ headspace glass vial filled with 10 cm³ of 10% KCl solution containing borosilicate glass beads, immediately capped with a gray butyl rubber septum, and sealed with an aluminum crimp cap. The vial was then vigorously shaken to help dissociate the sediment. Potassium chloride is toxic and was thus used to stop all microbial activity in the sediment. The glass beads (3 mm diameter) were used to help break up the sediment plug during shaking and liberate gas trapped in sediment pore space or adsorbed on particles. The vials were flushed with helium and capped within 1 h prior to sampling in order to remove air from the headspace and ensure the sample is preserved anaerobically. The objective is to preserve CO₂ from the interstitial water for stable carbon isotope analysis.

Headspace, NZ, and void gas samples were directly injected into the gas chromatograph–flame ionization detector (GC-FID) or into the NGA. The headspace samples were analyzed using an Agilent/HP 6890 Series II gas chromatograph (GC3) equipped with a 2.4 m × 3.2 mm stainless steel column packed with 100/120 mesh HayeSep R and a FID set at 250°C. The GC3 oven temperature was programmed to hold for 0.5 min at 80°C, ramp at 30°C/min to 100°C, ramp at 15°C/min to 110°C, and remain at 110°C for 4.5 min before ramping at 50°C/min to 150°C, with a final holding time of 1.8 min. Helium was used as the carrier gas. The GC3 system determines concentrations of methane (C₁), ethane (C₂), ethene (C₂₌), propane (C₃), and propylene (C₃₌). Alternatively, concentrations of C₁–C₆ hydrocarbons as well as nonhydrocarbons N₂, O₂, and CO₂ were measured using the NGA system. For hydrocarbon analysis, the NGA consists of an Agilent/HP 6890 Series II NGA equipped with an Agilent DB-1 dimethylpolysiloxane capillary column (60 m × 0.25 mm diameter × 0.25 μm film thickness) fitted with a FID and using helium as carrier gas (constant flow of 2 mL/min). The gas chromatograph oven temperature was programmed to hold for 2 min at 50°C, ramp at 8°C/min to 70°C, and then ramp at 25°C/min to 200°C with a final holding time of 5 min. The FID temperature was 250°C. For nonhydrocarbon gases, thermal conductivity detector (TCD) separation used three columns: a 6 ft × 2.0 mm internal diameter stainless steel column (Poropak T; 50/80 mesh), a 3 ft × 2.0 mm internal diameter stainless steel molecular

sieve column (13X; 60/80 mesh), and a 2.4 m × 3.2 mm internal diameter stainless steel column packed with 80/100 mesh HayeSep R (Restek).

Data were collected using the Hewlett Packard 3365 Chemstation data processing program. Chromatographic response is calibrated to nine different gas standards with variable quantities of low molecular weight hydrocarbons, N₂, O₂, CO₂, Ar, and He and checked on a daily basis. The gas concentrations for the required safety analyses are expressed as component parts per million by volume (ppmv) relative to the analyzed gas. The internal volumes of 15 representative headspace vials were carefully measured and determined to average 21.5 ± 0.18 mL. This volume was taken as a constant in calculations of gas concentrations.

The volumetric units were converted to millimolar concentration units (mM) to facilitate comparisons with dissolved interstitial water constituents as follows:

$$\text{CH}_4 = \chi_M \times P_{\text{atm}} \times V_H \times R^{-1} \times T^{-1} \times \phi^{-1} \times V_S^{-1},$$

where

- V_H = volume of the sample vial headspace,
- V_S = volume of the whole sediment sample,
- χ_M = molar fraction of methane in the headspace gas (obtained from gas chromatograph analysis),
- P_{atm} = pressure in the vial headspace (obtained from the bridge),
- R = the universal gas constant,
- T = temperature of the vial headspace in degrees Kelvin, and
- ϕ = sediment porosity (determined either from moisture and density [MAD] measurements on adjacent samples or from porosity estimates derived from gamma ray attenuation [GRA] data representative of the sampled interval).

Sediment geochemistry

To complement the interstitial water analyses, a cluster of subsamples was collected from a single whole round adjacent to the interstitial water whole round for sediment characterization. Shipboard measurements of cluster samples included geochemical analysis following procedures described below, as well as XRD, porosity, and bulk density analysis following procedures described in “**Lithostratigraphy and petrology**” and “**Physical properties.**” In addition, sediment subsamples were taken from the cluster for shore-based studies that include cation exchange capacity, biomarkers, major and minor element chemistry, high-pressure and -temperature experiments,

and isotopic characterization of iron and molybdenum (Table T5).

For the shipboard sediment geochemistry, 5 cm³ of sediment was freeze-dried for ~24 h, crushed to a fine powder using a pestle and agate mortar, and subsampled to analyze total carbon, total inorganic carbon and total nitrogen.

Elemental analysis

Total carbon and total nitrogen of the sediment samples were determined with a ThermoElectron Corporation FlashEA 1112 CHNS elemental analyzer equipped with a ThermoElectron packed column CHNS/NCS and a TCD. Approximately 10–15 mg of freeze-dried, ground sediment was weighed into a tin cup and the sample was combusted at 900°C in a stream of oxygen. The reaction gases were passed through a reduction chamber to reduce nitrogen oxides to nitrogen and were then separated by the gas chromatograph before detection by TCD. All measurements were calibrated to a standard, sulfanilamide, which was run every five samples. The detection limit was 0.001% for total nitrogen (instrument limit) and 0.002% for total carbon (procedural blank, measured as an empty tin cup).

Total inorganic carbon was determined using a Coulometrics 5011 CO₂ coulometer. Approximately 10–15 mg of freeze-dried, ground sediment was weighed into a glass vial and acidified with 2M HCl. The liberated CO₂ was titrated, and the corresponding change in light transmittance in the coulometric cell was monitored using a photodetection cell. The weight percent of calcium carbonate was calculated from the inorganic carbon (IC) content using the following equation:

$$\text{CaCO}_3 \text{ (wt\%)} = \text{IC (wt\%)} \times 100/12.$$

NIST-SRM 88b (Standard Reference Material) was used to confirm accuracy. Standard deviation for the samples and standards is less than ±0.1 wt%. Total organic carbon content was calculated by subtraction of inorganic carbon from total carbon.

Microbiology

Core handling and sampling

For all microbiological analysis conducted for this expedition, it was imperative to use proper, careful handling techniques. Subseafloor microorganisms are expected to be sensitive to chemical and physical changes caused by the relatively undisturbed conditions to which they are accustomed. Hence, great care was taken to avoid any unnecessary disturbance of the samples prior to analysis. After sectioning of

the core, whole-round subsamples were cut with a sterile spatula—or for highly compacted samples, separated from the rest of the core using a sterile chisel and hammer—capped, and taken to the Microbiology Lab for sampling. In the lab, all samples were immediately transferred to a cold storage room (<10°C) until further processing. Samples destined for oxygen-sensitive analyses were transferred into an anaerobic chamber within the cold room as soon as possible until processed. Whole-round samples were further subsampled for different microbiological methods. In all cases, sterile technique was a primary concern. Prior to subsampling, the whole-round sample was cleaned by removing the top ~1 cm of sediment with a flame-sterilized spatula. Immediately after cleaning, sterile, cut-off syringes (minicores) were pushed into the fresh surface of the whole round and samples were removed and stored as required for the different analyses. When sediment became too compacted to push the syringes in, subsamples were removed with a sterile spatula or chisel into Falcon tubes. The outer ~1 cm of the whole round, which was against the nonsterile core liner, was not used for subsampling. Minicore samples destined for shore-based DNA analysis were sealed into plastic bags and stored at –80°C for transportation to shore. Minicore samples for shore-based cultivation analysis were placed into polyester film bags, flushed three times with nitrogen, sealed under a nitrogen atmosphere to limit contamination of oxygen into the sample, and stored at 4°C. Minicores (3 cm³) taken for cell enumeration were extruded directly into a fixative solution containing 2% paraformaldehyde in sterile, filtered seawater. For these, only the middle 2 cm³ of the minicore was extruded into the fixative, to obtain the cleanest sample available.

Cell enumeration

The slurry produced by addition of sediment from the minicores or powdered samples to the fixative solution was shaken vigorously to disperse the sediment. A small aliquot of this slurry (50 µL) was filtered through a black 0.2 µm pore-size polycarbonate filter. Premixing of the aliquot with a few milliliters of sterile filtered seawater added to the filter tower apparatus ensured even distribution of the sample on the filter. The dry filter was then mounted on a glass slide with 20 µL of a staining solution and a glass coverslip. The staining solution consisted of SYBR Green I (1:40 dilution), glycerol, Vectashield mounting media, and phenylenediamine (1%) in a 3:3:3:1 volumetric ratio. Slides were incubated with the staining solution at room temperature in the dark for 1–2 h and stored in the freezer overnight be-

fore enumeration to reduce background fluorescence. Blanks were also prepared in the same way but omitting addition of sample. Cells were enumerated by the average number of SYBR Green I-stained particles in a microscopic field using an epifluorescence microscope (ZEISS Axioplan 2 imaging microscope), and images were taken with a ZEISS AxioCamHRc camera. The blanks provided an estimate of the level of background and/or contaminating cells, and final cell counts were adjusted accordingly.

Contamination analyses

During ODP Leg 201 (D'Hondt, Jørgensen, Miller, et al., 2003), contamination concerns for microbiological sampling of cores were addressed through the development of two separate tests for assessing contamination of the cores from the drilling processes: (1) the use of perfluorocarbon tracer added to the drilling fluid and (2) the use of microbe-size fluorescent microsphere beads introduced at the drill bit (Smith et al., 2000a, 2000b). For this expedition, contamination was assessed using the fluorescent microsphere test. Microspheres were deployed during XCB and RCB coring in any core from which microbiological samples were to be taken. Quantifying the number and lateral extent of microspheres introduced into the cores assessed contamination. Samples taken for this analysis were 3 cm³ minicores, when possible. When sediment was too compacted for minicores, samples were removed with a sterile spatula or chisel. All contamination samples were prepped in the same way as those for cell counting described above, except for the replacement of the staining solution with a simple solution of 1:1 phosphate-buffered saline and glycerol. Microspheres were enumerated by taking the average number in a microscopic field using an epifluorescence microscope. Microspheres were not deployed during APC coring because of concerns of physical damage to the core from the microsphere packaging; however, previous perfluorocarbon tracer tests of APC core have consistently shown that the centers of the APC cores are relatively pristine (House et al., 2003).

In addition to the shipboard checks, contamination will be further assessed postcruise by comparison of the microbial communities in the sediment samples with those in the drilling fluid using molecular methods. With these data, the genomic signatures of the contaminating drilling fluid microorganisms can sometimes be subtracted from those of the subsurface communities.

Physical properties

Physical property measurements provide fundamental information required to characterize lithostratigraphic units, properties of the upper basement, and

hydrogeology and allow for correlation of cored materials with LWD data. The primary objective of the Expedition 334 physical properties program was to collect high-resolution data to document the tectonically eroding Costa Rica margin offshore of the Osa Peninsula. A variety of techniques and methods were used to characterize Expedition 334 core samples.

Recovered whole-round cores were first allowed to thermally equilibrate to ambient room temperature of ~20°C (3 h for indurated material and 4 h for sedimentary material). After thermally equilibrating, core sections with continuous intervals longer than 8 cm were run through the Whole-Round Multi-sensor Logger (WRMSL) for measurement of GRA density, magnetic susceptibility, and compressional wave velocity (on the P-wave Logger [PWL]). The noncontact resistivity logger was not functional during Expedition 334. Sections longer than 50 cm were measured with the spectral Natural Gamma Ray Logger (NGRL).

After measurements with the WRMSL and NGRL, the cores were split into archive and working halves. The archive half of the core was passed through the SHMSL for measurement of point magnetic susceptibility. The SHMSL also uses a laser to record relief along the core, which yields information about the location of gaps and cracks between core pieces. This information was used to aid data filtering of whole-round and split-half measurements. Following the SHMSL, digital image scanning and color spectrophotometry were carried out on the cut surfaces of archive core halves using the SHIL and SHMSL, respectively.

Thermal conductivity was measured using the TeKa (Berlin, Germany) thermal conductivity meter. For cores with unlithified sediments, thermal conductivity measurements were carried out on whole-round core sections using the needle probe technique. For lithified sediments or indurated samples, thermal conductivity was measured on split cores using the half-space technique.

Discrete samples were taken from the working half at an interval of approximately every section. Discrete samples were used for compressional wave velocity in three directions and MAD measurements, including wet bulk density, dry bulk density, grain density, water content, void ratio, and porosity. A comprehensive discussion of methodologies and calculations used in the *JOIDES Resolution* Physical Properties Laboratory is presented in Blum (1997). Details about each physical property measurement are described below.

Whole-Round Multisensor Logger measurements

GRA bulk density and magnetic susceptibility were measured nondestructively with the WRMSL. To op-

timize WRMSL performance, sampling intervals and measurement integration times were the same for all sensors. Sampling intervals were set at either 2 or 5 cm, depending on core flow, with an integration time of 5 s for each measurement. These sampling intervals are common denominators of the distances between the sensors installed on the WRMSL (30–50 cm) and allow sequential and simultaneous measurements. GRA performance was monitored by passing a single core liner filled with deionized water through the WRMSL after every core.

In general, measurements are most effective with a completely filled core liner with minimal drilling disturbance. For sediment cores, the core liner with a 66 mm diameter was assumed filled. Basement sections are often recovered in pieces narrower than the core, which compounds the diameter discrepancy that is already introduced by the drilling process. Therefore, GRA bulk density and magnetic susceptibility measurements tend to underestimate true values. The data were filtered to remove anomalously low values associated with gaps and cracks in the core.

Gamma ray attenuation bulk density

The GRA densitometer on the WRMSL operates by passing gamma rays from a ^{137}Cs source through a whole-round core into a 75 mm \times 75 mm sodium iodide detector situated directly below the core. The gamma ray peak has a principal energy of 0.662 MeV and is attenuated as it passes through the core (Evans, 1965; Harms and Choquette, 1965). The attenuation of gamma rays, mainly by Compton scattering, is related to the material bulk density and thickness of sample. The gamma ray count is proportional to density. Bulk density, ρ , determined with this method can be expressed as

$$\rho = 1/(\mu d) \times \ln(I_0/I),$$

where

- μ = Compton attenuation coefficient,
- d = sample diameter,
- I_0 = gamma ray source intensity, and
- I = measured intensity of gamma rays passing through the sample.

The attenuation coefficient and gamma ray source intensity are treated as constants, such that ρ can be calculated from I . The gamma ray detector is calibrated with a set of aligned aluminum cylinders of various diameters surrounded by distilled water in a sealed core liner that is the same as that used during coring operations. The relationship between I and the product of μ and d can be expressed as

$$\ln(I) = A(\mu d)^2 + B(\mu d) + C,$$

where A , B , and C are coefficients determined during calibration. Gamma ray counts through each cylinder were determined for a period of 60 s, and the natural log of resulting intensities was plotted as a function of μd . Here, ρ of each aluminum cylinder was 2.7 g/cm³ and d was 1, 2, 3, 4, 5, or 6 cm. These coefficients fluctuated slightly during the time period over which the measurements were made, as indicated by repeated calibrations. The WRMSL provided the values of I and μ , and ρ was calculated with the above equation. Recalibration was performed as needed if the deionized water standard after every core deviated significantly (more than a few percent) from 1 g/cm³. The spatial resolution of the GRA densitometer is <1 cm.

Magnetic susceptibility

Magnetic susceptibility, k , is a dimensionless measure of the degree to which a material can be magnetized by an external magnetic field,

$$k = M/H,$$

where M is the magnetization induced in the material by an external field strength H . Magnetic susceptibility of the sediment responds to variations in the magnetic composition that commonly can be related to mineralogical composition (e.g., terrigenous versus biogenic materials) and diagenetic overprinting. Materials such as clay, possibly from alteration of igneous materials, have a magnetic susceptibility several orders of magnitude lower than magnetite and some other iron oxides that are common constituents of igneous material. Water and plastics (core liner) have a slightly negative magnetic susceptibility.

The WRMSL incorporates a Bartington Instruments MS2 meter coupled to a MS2C sensor coil with an 8.8 cm diameter and operates at a frequency of 565 Hz. The sensor output can be set to centimeter-gram-second (cgs) units or Systeme Internationale (International System; SI) units, with the IODP standard being the SI setting. The core diameter is smaller than the aperture through which it passes to be measured. Therefore, a volume correction factor must be applied to the data. Assuming a core diameter of 66 mm and using the coil aperture of 88 mm, the correction factor simply entailed multiplying the 10⁻⁵ SI units by a factor of 0.68 (Blum, 1997).

The instrument is calibrated with a homogeneous mixture of magnetite and epoxy in a 40 cm long piece of core liner to an accuracy of $\pm 5\%$. However,

this calibration is a factory preset. The resolution of the method is ± 4 cm; therefore, core material that is not continuous over an 8 cm interval will underestimate the magnetic susceptibility. Data collected near gaps or pieces smaller than 8 cm were removed by a simple filter.

Compressional *P*-wave velocity

P-wave velocity was measured on sediment cores. *P*-wave velocity varies with lithology, porosity, and bulk density of material; state of stress; temperature; and fabric or degree of fracturing. In sediment and rock, velocity is controlled by degree of consolidation and lithification. Because the contact between the core liners and hard rock samples is often poor, *P*-wave velocity was not measured on basement cores.

The PWL measures the ultrasonic *P*-wave velocity of the whole-round sample residing in the core liner. The PWL transmits a 500 kHz *P*-wave pulse across the core section at a specified repetition rate. This signal is coupled to the sample by the plastic pole contacts of the transducers clamped to the sides of the core by the linear actuator. No water is used to improve coupling between the transducers and the liner. The plastic pole contacts and the pressure applied by the actuator are sufficient for reliable *P*-wave measurement. The transmitting and receiving ultrasonic transducers are aligned so that wave propagation is perpendicular to the long axis of the core section. Torque applied by the actuator can be set by the user to ensure good acoustic contact between the liner and the core material.

The basic relationship for sonic velocity, V , is

$$V = d/t,$$

where d is the path length of the wave the core and t is the traveltime. The total traveltime between the transducers includes three components:

- t_{delay} (time delay related to transducer faces and electronic circuitry),
- t_{pulse} (delay related to the peak detection procedure), and
- t_{liner} (transit time through the core liner).

The system is calibrated using a core liner filled with pure water. For routine measurement on whole-round cores inside core liners, the corrected core velocity, V_{core} , can be expressed by

$$V_{\text{core}} = (d'_{\text{core}} - 2d_{\text{liner}})/(t_0 - t_{\text{pulse}} - t_{\text{delay}} - 2t_{\text{liner}}),$$

where

$$d'_{\text{core}} = \text{measured diameter of core and liner,}$$

$$\begin{aligned} d_{\text{liner}} &= \text{liner wall thickness, and} \\ t_0 &= \text{measured total traveltime.} \end{aligned}$$

Traveltime is determined by signal processing software that automatically detects first arrival of the *P*-wave signal to a precision of 50 ns. It is a challenge for an automated routine to pick the first arrival of a potentially weak signal if background noise is high. The search method skips the first positive amplitude and finds the second positive amplitude using a detection threshold limit, typically set to 30% of the maximum amplitude of the signal. The program then finds the preceding zero crossing and subtracts one wave period to determine the first arrival. To avoid extremely weak signals, minimum signal strength can be set (typically 0.02 V) and weaker signals are ignored. To avoid signal interference at the beginning of the record from the receiver, a delay (typically 0.01 ms) can be set to force the amplitude search to begin in the quiet interval preceding the first arrival. In addition, a trigger (typically 4 V) is selected to initiate the arrival search process, and the number of waveforms to be stacked (typically five) can also be set. A linear voltage differential transformer (LVDT) measures the separation of the transducer to derive a signal path length (i.e., the core diameter). After corrections for system propagation delay, liner thickness, and liner material velocity, the ultrasonic *P*-wave velocity is calculated.

Natural Gamma Radiation Logger

The NGRL installed on the *JOIDES Resolution* was designed and built at the Texas A&M University (USA) IODP facility between 2006 and 2008. The NGRL measures gamma radiation emitted from whole-round core sections arising primarily from the decay of ^{238}U , ^{232}Th , and ^{40}K isotopes.

The main NGR detector unit consists of 8 sodium iodide (NaI) scintillator detectors, 7 plastic scintillator detectors, 22 photomultipliers, and passive lead shielding. The NaI detectors are covered by 8 cm of lead shielding. In addition, lead separators (~7 cm of low-background lead) are positioned between the NaI detectors. Half of the lead shielding closest to the NaI detectors is composed of low-background lead, whereas the outer half is composed of regular (virgin) lead. In addition to passive lead shielding, the NGRL employs a plastic scintillator to suppress the high-energy gamma and muon components of cosmic radiation by producing a cancelling signal when these charged particles pass through the plastic scintillators. The NGRL was calibrated using a source consisting of ^{137}Cs and ^{60}Co and identifying the peaks at 662 keV (^{137}Cs) and 1330 keV (^{60}Co). Calibration materials are provided by Eckert and Ziegler Isotope Products (Valencia, California, USA).

For presentation purposes, the counts were summed over the range of 100–3000 keV and are thus comparable with data collection from previous cruises and direct comparison with downhole logging data. Background measurements of an empty core liner counted for 20,000 s (5 h) were made upon arrival at each site. Over the 100–3,000 keV integration range, background counts averaged 4–5 cps and contributed <0.5% to the overall signal of the measured core.

A measurement run consisted of eight measurements offset by 20 cm each. The quality of the energy spectrum measured in a core depends on the concentration of radionuclides in the sample but also on the counting time, with higher times yielding better spectra. The available count time in each position depended on how fast and how much of the core was recovered. In general, counting times were limited to 10 min, yielding statistically significant energy spectra.

Section Half Multisensor Logger measurements

The SHMSL measures magnetic susceptibility and spectral reflectance on core section halves. The archive half of the split core is placed on the system's core track. An electronic platform moves along a track above the core section, recording the sample height with a laser sensor. The laser establishes the location of the bottom of the section and the platform reverses the direction of movement, moving from bottom to top making measurements of point magnetic susceptibility and spectral reflectance data at 2 cm intervals.

Color reflectance spectrometry

Reflectance is measured from 171 to 1100 nm wavelength at 2 nm intervals using a halogen light source, covering a wavelength from ultraviolet through visible to near infrared. The scan of the entire wavelength range takes ~5 s per data acquisition offset. The data are generated using the L*a*b color system, in which L* is luminescence, a* is the blue + green value, and b* is the red + green value. The color reflectance spectrometer calibrates on two spectra, pure white (reference) and pure black (dark). Color calibration was conducted approximately every 12 h.

Point magnetic susceptibility

Point magnetic susceptibility is measured using a contact probe with a flat, 15 mm diameter sensor operating at a frequency of 0.580 kHz. The sensor takes and averages three measurements at 0.1 attenuation

for each offset to an accuracy of 5%. The spatial resolution of the magnetic susceptibility point instrument is 20 mm, making it advantageous over whole-round magnetic susceptibility for basement cores consisting of broken pieces <8 cm long (the spatial resolution of whole-round magnetic susceptibility). Units are reported in dimensionless SI units on a volume basis. The point magnetic susceptibility meter was calibrated by the manufacturer before installation on the ship. The probe is zeroed in air before each measurement point, and a background magnetic field is measured that includes the influence of the metal track and other sources. The background field was removed from the data before being output. The instrument is calibrated such that the value output is measured assuming the probe is buried into the sample; however, because the probe is only in contact with the upper, flat surface, a correction factor of two was applied after the data were collected. Note that the data stored in LIMS have not had this correction applied.

Thermal conductivity

Thermal conductivity is a measure of the ease with which heat flows through a material and is dependent on composition, porosity, and structure. Thermal conductivity was measured on unconsolidated sediment and rock samples using either the full-space needle probe (Von Herzen and Maxwell, 1959) or the half-space line source (Vacquier, 1985), respectively. Both the full- and half-space methods approximate the heating element as an infinite line source (Blum, 1997). These measurements produce a scalar value in a plane perpendicular to the orientation of the probe. All measurements were made after the cores had equilibrated to ambient laboratory temperature. At the beginning of each measurement, temperatures in the samples were monitored to ensure that the background thermal drift was <0.04°C/min. After the background thermal drift was determined to be stable, the heater circuit was closed and the increase in the probe temperature was recorded. In most cases the reported thermal conductivity value for full-space needle probe measurements is the average of at least three repeated measurements. For a half-space line source, thermal conductivity values typically represent the average of between five and ten repeated measurements. Based on these repeated measurements, individual measurements are usually within 1% of the mean for both full- and half-space measurements. Both of these values are within the stated uncertainty of 5% (Blum, 1997). All data are corrected to in situ pressure and temperature, assuming a hydrostatic pressure gradient and a background temperature gradient based on the advanced piston

corer temperature tool (APCT-3). The pressure correction is +1% for each 1800 m (Ratcliffe, 1960).

In porous rocks, temperature influences thermal conductivity in two competing ways. The thermal conductivity of rock matrix is inversely related to temperature (Zoth and Haenel, 1988), whereas the thermal conductivity of water increases with temperature (Keenan et al., 1978). The temperature correction is +1% for each +20°C change in temperature between the laboratory and in situ conditions, a value intermediate between +5% suggested by Ratcliffe (1960) for a high-porosity, water-saturated sediment and mean value of -3% derived from data reported by Clark (1966) for several hard rocks. Both uncorrected and corrected values of thermal conductivity are reported.

Soft-sediment full-space measurements

A full-space single-needle probe TeKa TK04 unit (Blum, 1997) was utilized to measure thermal conductivity of whole cores. To insert this probe, a 2 mm hole was made in the core liner at a position based on visual inspection of the core. Needle probes consist of a heater wire and a thermistor. At the beginning of each measurement, temperature in the sediment is monitored to ensure that the thermal drift does not exceed 0.4 mK/min. This step normally takes 1–2 min. After the temperature field is determined to be near equilibrium, a calibrated heat source is applied and the rise in temperature is recorded for ~80 s. Values of thermal conductivity are based on the observed rise in temperature for a given quantity of heat. In most cases, repeated measurements were made at the same location and in these the needle probe is left in place and the sample is left to reequilibrate for 10 min prior to the next measurement. Consequently, most of the time a measurement takes is waiting for the sample to reequilibrate.

Lithified sediment and hard rock half-space measurements

Thermal conductivity on basement samples was measured on the archive half of the split core with the thermal conductivity meter in half-space mode (Vacquier, 1985). Samples must be smooth to ensure adequate contact with the heating needle. Visible saw marks were removed when necessary by grinding and polishing the split surface with 120–320 gauge silicon carbide powder. Most samples did not require polishing. Basement samples equilibrated to room temperature in a seawater vacuum saturator for 4 h, and sample and sensor needle were equilibrated together in a cooler insulated with styrofoam for at least 15 min prior to measurement. Isolation of

the sample and sensor needle eliminated the effect of rapid but small temperature changes introduced by air currents in the laboratory. The instrument internally measures drift and does not begin a heating run until sufficient thermal equilibrium is attained. Cores were measured at irregular intervals (aiming for one sample per section) depending on the availability of homogeneous and relatively vein- and crack-free pieces long enough to be measured without edge effects (pieces at least 7 cm long; i.e., longer than the instrument needle).

Discrete sample measurements

Cubic samples were cut from the working halves of split cores at an interval of ~1 sample per section for both sediment and basement cores. These ~7 cm³ samples aimed to best represent the general variation and lithologies of the core. The purpose of these samples is twofold. First, they are used for physical property measurements of compressional wave velocity and MAD measurements (discussed below). Second, discrete samples were shared with paleomagnetists to minimize core depletion.

Moisture and density

Several basic quantities of interest (water content, bulk density, dry density, porosity, and void ratio) are found most accurately through mass and volume determinations on discrete samples. MAD data are also used for comparison with GRA bulk density data from the WRMSL. The shipboard MAD facility on the *JOIDES Resolution* includes a dual-balance system and a hexapycnometer. For hard rock samples, a vacuum water saturator is also used.

Vacuum water saturator

Basement samples were saturated in a vacuum pump system. Samples were placed in a plastic chamber filled with seawater. A vacuum pump removes the air from the chamber, drawing seawater into the samples. The samples were kept under saturation for at least 24 h. During this time, the vacuum was checked at 2–3 h intervals for possible leaks. After removal from the saturator, the cubes were stored in sample containers filled with seawater to help prevent evaporation of interstitial water. Next, the cube surfaces were patted dry with a paper towel, and wet mass was immediately determined using the dual-balance system.

Dual-balance system

The dual-balance system was used to measure both wet and dry masses. The two analytical balances,

Mettler-Toledo XS204, were used to compensate for ship motion, with one acting as a reference and the other for measurement of the unknown. A standard weight of similar value to the sample was placed upon the reference balance to increase accuracy. The default setting of the balances is 300 measurements (taking ~1.5 min).

Hexapycnometer system

The hexapycnometer system measures dry sample volume using pressurized, helium-filled chambers. At the start of the expedition and whenever the helium gas tank was changed, shipboard technicians performed a calibration using stainless steel spheres of known volume. A batch of samples consisted of four cells with unknowns and one cell with two stainless steel spheres (3 and 7 cm³). The spheres were cycled through the cells to identify any systematic error and/or instrument drift. Spheres are assumed to be known to be within 1% of their total volume. Individual volume measurements were preceded by three purges of the sample chambers with research grade (99.995% or better) helium heated to 28°C followed by three data acquisition cycles.

Wet and dry mass measurements

Immediately after sediment samples were collected or basement samples were saturated, the wet sediment mass (M_{wet}) was measured. Dry sediment mass (M_{dry}) and volume (V_{dry}) were measured after drying the samples in a convection oven for >24 h at a temperature of 105° ± 5°C. Dried samples were then cooled in a desiccator for >1 h before the dry mass was measured. Dry volume was measured using a helium-displacement pycnometer with a nominal precision of ±0.04 cm³. Each reported value consists of an average of three measurements.

For calculation of sediment bulk density, dry density, grain density, porosity, and void ratio, the traditional ODP method is used (Method C; Blum, 1997). Water content, porosity, and void ratio are defined by the mass or volume of extracted water before and after removal of interstitial water through the drying process. Standard seawater density (1.024 g/cm³) is used for the density of interstitial water. For basement samples that are too vesicular to saturate, we calculated these values using Method D (Blum, 1997), where wet mass is determined by caliper rather than by saturation.

Water content

Water content (W_c) was determined following the methods of the American Society for Testing and Materials (ASTM) designation D2216 (ASTM International, 1989). Corrections are required for salt when

measuring the water content of marine samples. In addition to the recommended water content calculation in ASTM D2216 (i.e., the ratio of interstitial-fluid mass to dry sediment mass [% dry weight]), we also calculated the ratio of interstitial-fluid mass to total sample mass (% wet wt). The equations for water content are

$$W_c (\% \text{ dry wt}) = (M_t - M_d)/(M_d - rM_t),$$

and

$$W_c (\% \text{ wet wt}) = (M_t - M_d) \times (1 + r)/M_t,$$

where

- M_t = total mass of the saturated sample,
- M_d = mass of the dried sample, and
- r = salinity.

Bulk density

Bulk density, ρ , is the density of the saturated samples, with $\rho = M_t/V_t$. The mass, M_t , was measured using the balance, and V_t was determined from the pycnometer measurements of grain volume and the calculated volume of the interstitial fluid ($V_t = V_{\text{pore}} + V_d$). For the high-porosity samples from Expedition 334, bulk density was determined directly from $\rho = M_t/V_t$.

Porosity

Porosity, ϕ , was calculated using

$$\phi = (W_c \times \rho)/[(1 + W_c) \times \rho_w],$$

where

- ρ = measured bulk density,
- ρ_w = density of the interstitial fluid, and
- W_c = water content expressed as a decimal ratio of percent dry weight.

Grain density

Grain density, ρ_{grain} , was determined from measurements of dry mass and dry volume made in the balance and in the pycnometer, respectively. Mass and volume were corrected for salt using

$$\rho_{\text{grain}} = (M_d - s)/[V_d - (s/\rho_{\text{salt}})],$$

where s is the salt content (in grams) and ρ_{salt} is the density of salt (2.257 g/cm³).

Compressional wave velocity

Discrete compressional wave (P -wave) velocity measurements were obtained on sediment cores at a fre-

quency of one per core. For basement samples, we used the same discrete cube samples that were also used for MAD and paleomagnetism determinations. *P*-wave measurements were performed on seawater-saturated samples directly after wet mass determinations were made. Measurements used the *x*-axis caliper-type contact probe transducers on the *P*-wave velocity gantry. Oriented samples were rotated manually to measure *y*- and *z*-axis velocities with the same instrument. The system uses Panametrics-NDT Microscan delay line transducers, which transmit at 0.5 MHz. To maximize contact with the transducers, deionized water was applied to sample surfaces.

The signal received through the sample was recorded by the computer attached to the system, and the peak of the initial arrival was chosen with autopicking software. The complete waveform is stored with the data if reanalysis is deemed necessary; however, visual checks of the picks made onboard appeared satisfactory. The distance between transducers was measured with a built-in LDVT.

Calibration was performed each day, before measurements were made, with a series of acrylic cylinders of differing thicknesses and known *P*-wave velocity of 2750 ± 20 m/s. The determined system time delay from calibration was subtracted from the picked arrival time to yield a traveltime of the *P*-wave through the sample. The thickness of the sample (calculated by LDVT in meters) was divided by the traveltime (in seconds) to calculate a *P*-wave velocity in meters per second.

Downhole temperature measurements

Downhole temperature measurements were made using the APCT-3 and the Sediment Temperature Tool (SET). The APCT-3 consists of three components: electronics, coring hardware, and computer software. The SET was developed by IODP based on the Davis-Villinger Temperature Probe design used in ODP and early IODP expeditions. Improved electronics and packaging provides high-resolution temperature measurements. The SET was used to take temperature measurements in stiffer formations. During this expedition, downhole temperature measurements were made for approximately every third core during APC coring. The temperature sensors were calibrated for a working range of 0° – 45° C.

Prior to entering a hole, each instrument is held at the mudline for ~5 min to equilibrate with bottom water temperature. After bottom water temperature equilibration, the tools are lowered in the hole to penetrate the formation. The penetration of each tool into the formation causes a rise in temperature

caused by frictional heating. Following the initial temperature rise, temperatures decrease along a decay curve to near equilibrium. During this decay phase, it is important that the temperature tool is not disturbed. A second rise in temperature is due to frictional heating as the tool is pulled out of the formation. Temperatures were measured as a time series with a sampling rate of 1 s and logged onto a microprocessor within the downhole tool. They were retrieved when the tool was recovered. The formation equilibrium temperature was determined based on fitting the temperature decay curve using the TP-Fit program, which runs on MATLAB (M. Heeseman et al., pers. comm., 2008)

Shear strength

Undrained shear strength was measured using the automatic vane shear (AVS) and a pocket penetrometer. The measurements were not performed at in situ stress conditions and thereby underestimate the true undrained peak shear strength in situ. All shear strength measurements were performed in the *y*–*z* plane.

Automatic vane shear system

Undrained shear strength (τ_{ru}) was measured in fine-grained, plastic sediment using the AVS system following the procedures of Boyce (1977). The vane rotation rate was set to 90° /min. Peak undrained shear strength was measured typically once per core. The instrument measures the torque and strain at the vane shaft using a torque transducer and potentiometer. The peak shear strength was determined from the torque versus strain plot. The experiment was set up to run for 6 min, which is 1.5 vane laps. Care was taken to conduct tests in undisturbed and homogeneous parts of the core. To minimize disturbance effects resulting from the measurement itself, vane shear tests were generally conducted first, followed by penetrometer tests. Measurements were made with the vane rotation axis and penetrometer penetration direction perpendicular to the split surface. The residual shear strength was taken to be the lowest measured shear strength after reaching the peak value during the test cycle. All shear strengths were measured with the rotation axis parallel to the bedding plane.

Vane shear strength, $S_{u(v)}$ (kPa), is calculated as

$$S_{u(v)} = T/K_v$$

where T is the torque required to fail the material (N·m) and K_v is the constant depending on vane dimensions (cubic meters) (Blum, 1997).

All measurements reported here were obtained using a vane with a height and diameter of 12.7 mm. Failure torque was determined by measuring the degrees of rotation of one of four torsional springs and a linear calibration equation (manufacturer specified) relating the rotation angle to torque for the particular spring being used. Selection of the appropriate spring was based on the anticipated shear strength of the material. Vane shear results were generally considered reliable for shear strength values less than ~150–200 kPa, above which excessive cracking and separation of the core material occurred.

Penetrometer

A pocket penetrometer (Geotester STCL-5) was used to obtain additional undrained shear strength measurements. The penetrometer is a flat-footed, cylindrical probe that is pushed 6.4 mm into the split-core surface. The penetrometer is calibrated as an unconfined compression test, which (for an ideal clay) measures twice the undrained shear strength, or $2\tau_{ru}$ (Holtz and Kovacs, 1981). The scale on the dial is converted into shear strength (in kilopascals) using [Blum, 1997]

$$2\tau_{ru} \text{ (kPa)} = 98.1 \times 2S_u \text{ (kg/cm}^2\text{)},$$

where τ_{ru} is undrained shear strength (kPa) and S_u is the penetrometer reading (kg/cm²).

Penetrometers are designed for use in soft sediment, and readings were discarded if the sediment cracked during measurement. Measurements using the penetrometer were typically performed once per core.

Paleomagnetism

Shipboard paleomagnetism was investigated mainly to determine directions of remanence components. Routine measurements were made on archive section halves with stepwise alternating-field (AF) demagnetization. Discrete cube and minicore samples were taken from working halves and measured with stepwise AF and thermal demagnetization for selected sections. These data were used for core reorientation and magnetostratigraphic studies.

Coordinates

All magnetic data are reported relative to the IODP orientation conventions: $+x$ is into the face of the working half, $+y$ points toward the left side of the face of the working half, and $+z$ is down. The relationship of the superconducting rock magnetometer (SRM) coordinate (X, Y, Z) to the data coordinate (x, y, z) for archive halves is $x = X, y = -Y,$ and $z = Z$ and

for working halves is $x = -X, y = Y,$ and $z = Z$ (Fig. F14).

Magnetic measurements

Remanent magnetization was measured using a 2G SRM (2G Enterprises model 760R). The noise level of the measurement system was routinely checked using the SRM Noise Monitor software, which was originally developed by Jeff Gee. The noise has the dominant frequency of wave motion (on the order of 0.1 Hz). The magnitude of noise was $\sim 5 \times 10^{-10}$ Am², and it was the same between tests with 1 and 10 Hz SRM electronics filters (2G model 581), because the dominant frequency of the noise was < 1 Hz. This noise corresponds to $\sim 5 \times 10^{-5}$ A/m noise for a half core. We decided to use a 10 Hz filter, instead of the commonly used 1 Hz filter, to obtain a faster response of the SRM to changes in magnetic signal. This may improve the measurements around the areas with sharp changes in magnetization (e.g., core ends), although pilot tests using a concrete core on the *JOIDES Resolution* revealed essentially no difference between 1 and 10 Hz filters (Fig. F15). Discrete samples were also measured using a spinner magnetometer (AGICO model JR-6A) when the cryogenic magnetometer was in use for long-core pass-through measurements. Ocean drilling cores generally carry secondary overprint remanence components. Common overprints for ocean drilling cores include natural viscous remanence and a steep downward-pointing component attributed to the rotating drill strings. To separate these from the characteristic remanent magnetization (ChRM), stepwise demagnetization experiments were performed, as described below.

Archive halves

Measurements of archive halves were conducted using the SRM software (version 3.18) with a 15.59 cm² nominal sample area parameter. The intervals between measurement points and measurement speed were selected as 2, 5, or 10 cm and 2–10 cm/s, respectively, depending on the available time and the magnetic character of the samples.

We performed successive AF demagnetization using the in-line SRM AF demagnetizer (2G Enterprises model 2G600) on all split-core archive sections. The in-line AF demagnetizer applies a field to the X -, Y -, and Z -axes of the SRM in this fixed order. We noticed that the AF demagnetizer produces anomalous demagnetization results after 50 mT demagnetization, as shown by uniform -90° inclination for the whole-core section. Previous reports suggest that higher AF demagnetization fields have produced significant anhysteretic remanent magnetization along the Z -axis

of the SRM. Given this limitation, we used demagnetization steps up to 40 mT for demagnetizing tray and sections. For most of the sediment sections, we only performed steps to 15–30 mT; for long pieces from basement sections, we performed progressive AF demagnetization to 15 mT because of time constraints. The AF demagnetization results were plotted individually as vector plots (Zijderveld, 1967) as well as downhole variations with depth. The response curve from the sensor coils of the SRM corresponds to a region ~20 cm wide; therefore, only measurements taken greater than 20 cm are independent from each other (Fig. F15). Measurements at core and section ends, whole-round locations and voids, and within intervals of drilling-related core disturbance were either not measured or were removed during data processing. We then inspected the plots visually to judge whether the remanence after demagnetization at the highest AF step reflects the ChRM and geomagnetic polarity sequence.

Discrete samples from working halves

Oriented discrete samples representative of the lithology were collected during the expedition. In soft sediments, cubic samples (~8 cm³) were taken by pressing plastic cubes into the split face of the working halves. In lithified sediments and hard rocks, minicores (~11 cm³) were taken. Measurements of discrete samples were conducted using the SRM software (version 3.18). For the JR6 spinner magnetometer, we used the REMA6 software. For approximately half of the discrete samples, we performed successive AF demagnetization with the DTech AF demagnetizer (model D-2000) for the spinner measurements. The remaining half of the discrete samples were demagnetized with the in-line AF demagnetizer and used for the SRM measurements. For selected discrete samples, we also performed successive thermal demagnetization using a thermal demagnetizer (Schonstedt model TSD-1). Temperature increments of 25° or 50°C were used depending on the unblocking temperature of each sample. We analyzed the stepwise demagnetization data of the discrete samples by principal component analyses to define the ChRM (Kirschvink, 1980).

Core orientation

Core orientation of APC cores was achieved with the Flexit orientation tool mounted on the core barrel. The tool consists of three mutually perpendicular fluxgate magnetic sensors and two perpendicular gravity sensors. The information from both sets of sensors allows the azimuth and dip of the hole to be measured, as well as the azimuth of the APC core ori-

entation. Generally, the Flexit tool has an accuracy of 20°–30°. The orientation information contributed to paleomagnetic polarity determinations and magnetostratigraphic interpretations.

The ChRM provides a reference frame to reorient cores (see “**Structural geology**”). Provided that the reference magnetic pole is known, the orientation of the paleomagnetic vector is then used to restore the azimuth of the core. The horizontal component of the mean ChRM makes an angle with the reference line, which specifies the rotation of the core relative to the geographic coordinates (e.g., Fuller, 1969). The relatively young expected age (Neogene) of the sediments and nearly longitudinal (westward) slow motion of the Caribbean plate during this period (e.g., Pindell et al., 1988) indicate that we can approximate the reference magnetic pole by the present-day geographic poles for the entire sediment section. The other assumptions for the reorientation are

1. The section has enough measurements to average out geomagnetic secular variation,
2. The original bedding is horizontal,
3. Core is vertical, and
4. The sedimentary unit has not experienced any vertical axis rotations.

Assumptions 2 and 3 were checked with shipboard structural geologists, seismic profiles of the drill sites, and drilling operational records.

For intervals of particular interest for structural geology, we reported ChRMs defined from discrete samples in the interval. More detailed demagnetization steps for the discrete samples allow more accurate ChRMs than those from the archive halves.

Magnetostratigraphy

Magnetostratigraphy for each site was constructed by correlating obtained geomagnetic polarity sequences with the geomagnetic polarity timescale of Gradstein et al. (2004) (Table T6). Expedition 334 drill sites are located at low latitude (~9°N), resulting in very small differences in inclinations between reversed and normal geomagnetic polarity. Consequently, defining paleomagnetic polarity and magnetostratigraphy from magnetic measurements alone was difficult for RCB and XCB cores, and biostratigraphic age constraints were incorporated to judge the correlation with the geomagnetic polarity timescale.

Whenever possible, we offer an interpretation of the magnetic polarity, following naming convention of correlative anomaly numbers prefaced by the letter C (Tauxe et al., 1983). Normal polarity subchrons are referred to suffixes (e.g., n1, n2, etc.) that increase

with age. For the younger part of the timescale (Pliocene–Pleistocene), we use traditional names to refer to the various chrons and subchrons (e.g., Brunhes, Jaramillo, Olduvai, etc.). In general, polarity reversals occurring at core ends have been treated with extreme caution because of the edge effects caused by the coring-related disruptions.

Downhole logging

The Expedition 334 downhole logging program was designed to complement the core sample record by measuring continuous in situ profiles of physical properties such as bulk density, porosity, resistivity, and NGR. In addition to these formation properties, downhole logging provides oriented images of the borehole wall that are useful in determining the directions of bedding planes, fractures, and borehole breakouts. With the conventional technique of wireline logging, downhole measurements are taken by tools lowered in a previously drilled borehole. Wireline logging has had limited success in deep holes in unconsolidated or fractured clastic sequences because these holes tend to be unstable after drilling. It may be difficult to lower wireline tools in an unstable borehole, and hole irregularity can compromise the quality of the measurements. Using LWD, downhole measurements are taken by instrumented drill collars in the BHA near the drill bit. Hence, LWD measurements are made shortly after the hole is drilled and before the adverse effects of continued drilling or coring operations. LWD has been successful in previous scientific drilling expeditions to convergent margins, such as Barbados (ODP Legs 156 and 171A), Costa Rica off Nicoya Peninsula (ODP Leg 170), and Nankai Trough (ODP Leg 196 and IODP Expeditions 314, 319, and 332) (Shipley, Ogawa, Blum, et al., 1995; Moore, Klaus, et al., 1998; Kimura, Silver, Blum, et al., 1997; Mikada, Becker, Moore, Klaus, et al., 2002; Kinoshita, Tobin, Ashi, Kimura, Lallemand, Screatton, Curewitz, Masago, Moe, and the Expedition 314/315/316 Scientists, 2009; Saffer, McNeill, Byrne, Araki, Toczko, Eguchi, Takahashi, and the Expedition 319 Scientists, 2010; Kopf, Araki, Toczko, and the Expedition 332 Scientists, 2011). LWD was selected as the logging technique for Expedition 334. The LWD equipment used during this expedition was provided by Schlumberger Drilling and Measurements under contract with the Lamont-Doherty Earth Observatory Borehole Research Group (LDEO-BRG).

Logging-while-drilling tools

LWD tools are supplemented by a measurement-while-drilling (MWD) tool that is located in the midst of the LWD tools in the BHA and measures

downhole drilling parameters and well bore direction. The MWD tool also transmits a limited LWD data set by acoustic telemetry to the surface for real-time monitoring. Complete LWD data are recorded into downhole computer memory and retrieved when the tools are brought to the surface. The term LWD is often used generically to cover both LWD- and MWD-type measurements, tools, and systems, and we follow this convention here.

LWD tools are powered by batteries or a drilling fluid turbine and store logging data in nonvolatile memory chips. The tools take measurements at regular time intervals and are synchronized with an acquisition system on the drilling rig that matches time with drilling depth. Drilling depth is determined using a drawworks encoder that measures the vertical motion of the top drive. After drilling, the LWD tools are retrieved and their data downloaded. The Schlumberger Maxwell logging system merges time-depth data (from the surface system) and the downhole time-measurement data (from the tools) into depth-measurement data files. Data files are then transferred to LDEO-BRG onshore for further processing. Processing includes depth shift to the seafloor, corrections to certain logs, documentation (with an assessment of log quality), and conversion of the data to ASCII format for the conventional logs and to GIF for the images. Schlumberger GeoQuest's GeoFrame software package is used for most of the processing. The data are transferred back to the ship within a few days of logging and made available in ASCII and DLIS formats through the shipboard IODP logging database.

The Schlumberger LWD tools used during Expedition 334 were the geoVISION 675 (near-bit electrical resistivity, resistivity images, and NGR), the arcVISION 675 (annular borehole pressure, resistivity, and NGR), the adnVISION 675 (neutron porosity and azimuthal measurements of ultrasonic caliper and of bulk density), and the MWD TeleScope 675 (drilling mechanics data and real-time telemetry). All of these tools had a 6¾ inch (17.1 cm) diameter and were located above an 8½ inch (21.6 cm) drill bit. Some tools had stabilizers to centralize the collars and keep measurement sensors near the borehole wall. Figure F16 shows the configuration of the LWD BHA, with the depth of the measurements relative to the bit, and Table T7 lists the principal measurements recorded by each tool. The measurement principles of these LWD tools are described below. More detail on the physical principles and methods of downhole logging is given by Ellis and Singer (2007).

geoVISION tool

The geoVISION resistivity tool (also known as resistivity at the bit) provides laterolog-type resistivity

measurements of the formation and high-resolution electrical resistivity images of the borehole wall. The tool uses two transmitter coils and a number of electrodes to obtain several measurements of resistivity (Bonner et al., 1996):

- **Bit resistivity:** the lower transmitter coil generates a current that flows through the bit and into the formation, returning to the drill collar far up the tool string. By measuring the axial current through the bit for a given voltage, resistivity near the bit is determined by Ohm's law.
- **Ring resistivity:** the upper and lower transmitter coils produce currents in the collar that flow out of the tool at the ring electrode. In a homogeneous medium, these currents flow perpendicular to the tool. In a heterogeneous formation, this radial current flow is distorted and the current pattern generated by the upper and lower transmitters is adjusted to focus current flow into the formation. A high-resolution resistivity measurement is taken by measuring the amount of current leaving the tool at the 4 cm thick ring electrode.
- **Button resistivity:** the same focusing process used in measuring the ring resistivity is applied to determine the resistivity at three 1 inch (2.5 cm) button electrodes. Button resistivity measurements made as the tool rotates in the borehole are stored and processed to produce a resistivity image of the borehole wall. The button electrodes measure resistivity at three depths of investigation and thus generate three resistivity images: shallow, medium, and deep. The tool uses the geomagnetic field to orient the resistivity images to magnetic north.

During Expedition 334, the geoVISION tool sampled image data every 5 s and the resistivity images were computed at 1 inch (2.5 cm) intervals. To maximize the spatial resolution of the images, the recommended rate of penetration is 2.5 cm every 5 s, or 18.3 m/h. Images with adequate spatial resolution, however, can be acquired at lower drilling rates, trading off resolution for drilling time.

The geoVISION tool also contains a scintillation detector that provides an azimuthal NGR measurement. The NGR log is indicative of clay content in a clastic sedimentary sequence because sands typically have a relatively low content of radioactive elements compared to clay minerals.

adnVISION tool

The adnVISION tool (azimuthal density neutron) measures bulk density, neutron porosity, and borehole diameter (Evans et al., 1995). As the tool rotates, it acquires data in azimuthal sectors around the borehole. The density section of the tool uses a

^{137}Cs gamma ray source and a near and a far scintillation detector that provide a borehole-compensated measurement. The density source and detectors are positioned in the fin of an 8.5 inch (20.6 cm) stabilizer. This geometry forces the sensors against the borehole wall, thereby reducing the effects of borehole irregularities. Whereas high-energy Compton scattering of gamma rays is a function of the bulk density, returns of scattered low-energy gamma rays also depend on the atomic number and are converted to a photoelectric effect (PEF) measurement that is sensitive to lithology. In a clastic sequence, PEF will be lower in sand-rich intervals (the PEF of quartz is 1.8 b/e⁻) and higher in intervals containing clay, mostly because of Fe in clay minerals (Fe has a high PEF of 31.2 b/e⁻) (Ellis and Singer, 2007).

Neutron porosity measurements are obtained by emitting high-energy fast neutrons from an americium oxide beryllium (AmBe) source and measuring low-energy epithermal and thermal neutrons in near- and far-spacing detectors. Hydrogen nuclei have a mass close to that of neutrons and are most efficient in slowing the fast neutrons emitted by the source. The neutron log estimates porosity from the density of hydrogen nuclei and gives an accurate porosity in clean formations (e.g., quartz sands) where almost all hydrogen is in formation waters. Conversely, hydrogen in clay mineral hydroxyls contributes to the slowing of neutrons and results in an overestimate of porosity in shales (Ellis, 1986).

The adnVISION tool measures tool standoff and borehole diameter with an ultrasonic caliper. In addition, the adnVISION computes an azimuthal density caliper based on the differences in density determined by the near and far detectors, which have different sensitivities to the standoff between the tool and the borehole (Labat et al., 2002). A standoff of <1 inch (2.5 cm) between the tool and the borehole wall indicates good borehole conditions, for which the density log values are considered to be accurate to $\pm 0.015 \text{ g/cm}^3$. The azimuthal density measurements are processed to obtain full-coverage images of bulk density and borehole radius. The images display 8 or 16 azimuthal measurements of density and borehole radius (from density and ultrasonic measurements).

arcVISION tool

The arcVISION tool (array resistivity compensated) measures propagation resistivities. Electromagnetic waves are attenuated and phase-shifted when they propagate in an electrically conductive medium, and the degree of attenuation and phase shift depends on the resistivity of the formation (Bonner et al., 1995, 1996). Phase-shift resistivity has relatively

high vertical resolution and a shallow depth of investigation, whereas attenuation resistivity has lower vertical resolution and a greater depth of investigation. The dual-frequency (2 MHz and 400 kHz) array of coils in the arcVISION makes 10 phase-shift and 10 attenuation measurements at five transmitter-receiver separations of 16, 22, 28, 34, and 40 inches (40.6, 55.9, 71.1, 86.4, and 101.6 cm), which correspond to several depths of investigation. For a given frequency, the vertical resolutions of phase-shift resistivities measured at different transmitter-receiver separations are similar. The arcVISION also measures the NGR of the formation and the pressure of the borehole fluid in the annulus (the space between the drill string and the borehole wall). During Expedition 334, the annular pressure measurement was monitored while drilling for safety (see below).

TeleScope tool

The TeleScope MWD tool transmits data uphole through the fluid in the drill pipe in a process known as “mud-pulse telemetry.” A modulator in the tool generates a continuous 12 Hz pressure wave within the drilling fluid and changes the phase of this signal to transmit bit words encoding various measurements made by the MWD tool or by other LWD tools in the BHA. Two pressure transducers attached to the standpipe (one near the top and a second near the bottom) on the rig floor acquire the pressure signal that is then decoded by the Schlumberger surface software. The MWD real-time data transmission rate is adjustable, depending primarily on water depth and drilling fluid density, and was 6 bits/s during Expedition 334.

In addition to transmitting uphole selected measurements from the other LWD tools, the TeleScope acquires operational and drilling mechanics data, including collar rotation per minute, drilling fluid turbine rotation per minute, stick and slip, and axial and torsional vibration. The TeleScope also contains a turbine that powers the entire LWD string when drilling fluid is circulated at a sufficient flow rate (~300 gal/min, or 18.9 L/s, in the TeleScope tool used during Expedition 334).

Gas monitoring with real-time LWD data

During Expedition 334, LWD logs were acquired in the first hole drilled at each site. As these holes were drilled without coring, the LWD data had to be monitored to detect gas entering the well bore. This LWD monitoring procedure substitutes the IODP standard of using gas ratio measurements made on cores for hydrocarbon safety analysis (Pimmel and Claypool,

2001). The LWD monitoring protocol used during Expedition 334 was similar to protocols used during previous IODP expeditions where LWD holes were drilled before coring, such as IODP Expeditions 308 (Gulf of Mexico hydrogeology) and 311 (Cascadia margin gas hydrates) (Flemings, Behrmann, John, and the Expedition 308 Scientists, 2006; Riedel, Collett, Malone, and the Expedition 311 Scientists, 2006).

The primary measurement used for gas monitoring was annular pressure while drilling, measured downhole and transmitted to the surface in real time by the arcVISION LWD tool. Free gas in the borehole lowers the borehole fluid density and decreases the pressure. The monitoring procedure consisted primarily in monitoring variations of annular pressure while drilling over a baseline hydrostatic pressure trend. A sustained drop in pressure greater than a specified threshold required drilling to stop and circulation of a full volume of the borehole annulus while monitoring pressure. If the pressure remained static and equal to the hydrostatic pressure trend, drilling could be resumed. If the pressure was lower than hydrostatic, the protocol required killing the hole with weighted mud and abandoning the hole.

The threshold pressure drops requiring attention were defined from a pressure decrease chosen to ensure that gas flow in the well could be killed with weighted mud. The threshold pressure drops were 30 psi (0.207 MPa) in the 0–100 mbsf interval, 35 psi (0.241 MPa) in the 100–200 mbsf interval, and 50 psi (0.345 MPa) in the 200–1000 mbsf interval.

Pressure decreases caused by gas flow into the borehole may also be preceded by a pressure increase as the result of acceleration of fluids in the annulus (e.g., Aldred et al., 1998). The protocol required close monitoring of the annular pressure if pressure increases over the hydrostatic trend were observed. Such a pressure increase could be the result of the aforementioned precursor or be induced by drilling (e.g., mud sweeps or packing off of cuttings). A drilling-induced pressure increase would be resolved by cleaning the hole, whereas the gas flow precursor event would be followed by a pressure decrease, leading to appropriate response as in the procedure above.

Gas flow into the borehole should cause a sustained decrease in annular pressure. There could also be occasional, brief pressure drops that are not caused by gas entry but are induced by drilling (e.g., pressure drops caused by flushing cuttings out of the hole). These transient pressure drops did not require the preventive actions described above.

Interpretation of LWD data

Log characterization and logging units

LWD logs provide in situ petrophysical information on the rock formation and interstitial water while the hole is being drilled. These measurements are sensitive to changes in formation properties such as composition, texture, and structure. Compositionally influenced logs such as NGR and PEF were used to estimate lithologic variation with depth. Borehole images provided useful information on geological features such as bedding, sedimentary structures, bed boundaries, unconformities, fractures, and faults. The characterization of logging data allows the borehole to be zoned into distinct logging units based on intervals of different log responses that are commonly associated with lithostratigraphic units. For Expedition 334, the aim was to provide a preliminary assessment of formation properties and lithostratigraphy from LWD data prior to coring.

Structural and breakout analyses from borehole images

The LWD tools used during Expedition 334 collected full-coverage borehole images of electrical resistivity, NGR (geoVISION), bulk density, and borehole radius from density and ultrasonic measurements (adnVISION). These images are typically plotted as an unwrapped cylindrical borehole wall and are referred to true north using a magnetic compass in the tools (Fig. F17). The resistivity images have the highest spatial resolution and can be used to map bedding planes, sedimentary structures, and fractures.

On unwrapped images taken in a vertical borehole, horizontal planes (e.g., bed boundaries) show up as horizontal straight lines, whereas dipping planes (e.g., fractures) as sinusoidal curves (Fig. F17). The dip direction is the azimuth of the lowest point in the sinusoidal curve, and the dip angle is $\tan^{-1}(h/d)$, where h is the amplitude of the sinusoidal curve and d is the borehole diameter. The interpretation of a large number of dipping planes can be aided by software that lets the user fit sinusoidal curves to features in the images (e.g., the BorView module in Schlumberger GeoQuest's GeoFrame software package).

Resistivity image data were displayed as statically and dynamically normalized images. Static normalization displays the image with a color range covering all resistivity values for the entire logged interval; this displays absolute changes in resistivity throughout the borehole and is useful for identifying lithologic or facies changes. Dynamic normalization

scales the color range for resistivity values in a moving depth window (1 m), highlights small-scale, subtle variations in resistivity, and is commonly used for detailed identification of fractures and formation structures.

Borehole breakouts are subvertical hole enlargements that form on opposite sides of the borehole wall by local drilling-induced failure caused by non-uniform stress. In a vertical borehole, the breakout direction is parallel to the minimum principal horizontal stress orientation and perpendicular to the maximum principal horizontal stress orientation (Bell and Gough, 1983). Therefore, borehole breakouts are key indicators of the state of stress in the subsurface. LWD images of resistivity and borehole radius clearly display borehole breakouts as two parallel, vertical bands of low resistivity or large borehole radius 180° apart. Borehole breakouts were mapped using GeoFrame software, and further quantitative analysis can be conducted postexpedition.

Core-log-seismic integration

To correlate core and log data acquired at depth with seismic reflection measurements that are a function of traveltime, a depth-traveltime relationship must be determined at each drill site. This relationship can be estimated with synthetic seismograms, which are computed by convolving a seismic impulse function with reflection coefficients obtained from contrasts in P -wave velocity and density. These velocities and densities may be measured in situ with downhole logs or on cores in the physical properties laboratory. Synthetic seismograms can be calculated using seismic interpretation packages. For example, IESX, part of the Schlumberger GeoFrame software suite, allows interactive adjustment of the depth-traveltime relationship until a good match is achieved between reflectors in the synthetic seismogram and in the measured seismic data. While P -wave velocities were not measured by the suite of LWD tools deployed during Expedition 334, velocities measured on cores and LWD densities could be combined to estimate reflection coefficients. Should the quality of the shipboard core and LWD measurements be sufficient, synthetic seismograms can be produced postexpedition.

References

- Aldred, W., Cook, J., Bern, P., Carpenter, B., Hutchinson, M., Lovell, J., Rezmer-Cooper, I., and Leder, P.C., 1998. Using downhole annular pressure measurements to improve drilling performance. *Oilfield Rev.*, 10(4):40–55. http://www.slb.com/~media/Files/resources/oilfield_review/ors98/win98/using.ashx

- ASTM International, 1990. Standard method for laboratory determination of water (moisture) content of soil and rock (Standard D2216–90). In *Annual Book of ASTM Standards for Soil and Rock* (Vol. 04.08): Philadelphia (Am. Soc. Testing Mater.). [revision of D2216-63, D2216-80]
- Bandy, O.L., and Arnal, R.E., 1957. Distribution of Recent foraminifera off the west coast of Central America. *AAPG Bull.*, 41:2037–2053.
- Bell, J.S., and Gough, D.I., 1983. The use of borehole breakouts in the study of crustal stress. In Zoback, M.D., and Haimson, B.C. (Eds.), *Hydraulic Fracturing Stress Measurements*: Washington (Natl. Acad. Press), 201–209.
- Berggren, W.A., Hilgen, F.J., Langereis, C.G., Kent, D.V., Obradovich, J.D., Raffi, I., Raymo, M.E., and Shackleton, N.J., 1995a. Late Neogene chronology: new perspectives in high-resolution stratigraphy. *Geol. Soc. Am. Bull.*, 107(11):1272–1287. doi:10.1130/0016-7606(1995)107<1272:LNCNPI>2.3.CO;2
- Berggren, W.A., Kent, D.V., Swisher, C.C., III, and Aubry, M.-P., 1995b. A revised Cenozoic geochronology and chronostratigraphy. In Berggren, W.A., Kent, D.V., Aubry, M.-P., and Hardenbol, J. (Eds.), *Geochronology, Time Scales and Global Stratigraphic Correlation*. Spec. Publ.—SEPM (Soc. Sediment. Geol.), 54:129–212.
- Blow, W.H., 1969. Late middle Eocene to Recent planktonic foraminiferal biostratigraphy. *Proc. Int. Conf. Planktonic Microfossils*, 1:199–422.
- Blum, P., 1997. Physical properties handbook: a guide to the shipboard measurement of physical properties of deep-sea cores. *ODP Tech. Note*, 26. doi:10.2973/odp.tn.26.1997
- Boggs, S., Jr., 2005. *Principles of Sedimentology and Stratigraphy* (4th ed.): Saddle River, NJ (Prentice-Hall).
- Bonner, S., Fredette, M., Lovell, J., Montaron, B., Rosthal, R., Tabanou, J., Wu, P., Clark, B., Mills, R., and Williams, R., 1996. Resistivity while drilling—images from the string. *Oilfield Rev.*, 8(1):4–19. http://www.slb.com/~media/Files/resources/oilfield_review/ors96/spr96/composite.ashx
- Bonner, S.D., Tabanou, J.R., Wu, P., Seydoux, J.P., Moriarty, K.A., Seal, B.K., Kwok, E.Y., and Kuchenbecker, M.W., 1995. New 2-MHz multiarray borehole-compensated resistivity tool developed for MWD in slim holes. *Proc.—SPE Annu. Tech. Conf.*, Pap. SPE 30547.
- Boyce, R.E., 1977. Deep Sea Drilling Project procedures for shear strength measurement of clayey sediment using modified Wykeham Farrance laboratory vane apparatus. In Barker, P.F., Dalziel, I.W.D., et al., *Init. Repts. DSDP*, 36: Washington, DC (U.S. Govt. Printing Office), 1059–1068. doi:10.2973/dsdp.proc.36.1977
- Bukry, D., 1973. Low-latitude coccolith biostratigraphic zonation. In Edgar, N.T., Saunders, J.B., et al., *Init. Repts. DSDP*, 15: Washington, DC (U.S. Govt. Printing Office), 685–703. doi:10.2973/dsdp.proc.15.116.1973
- Bukry, D., 1975. Coccolith and silicoflagellate stratigraphy, northwestern Pacific Ocean, Deep Sea Drilling Project Leg 32. In Larson, R.L., Moberly, R., et al., *Init. Repts. DSDP*, 32: Washington, DC (U.S. Govt. Printing Office), 677–701. doi:10.2973/dsdp.proc.32.124.1975
- Clark, S.P. (Ed.), 1966. *Handbook of Physical Constants*. Mem.—Geol. Soc. Am., 97.
- Crouch, R.W., and Poag, C.W., 1987. Benthic foraminifera of the Panamanian Province; distribution and origins. *J. Foraminiferal Res.*, 17(2):153–176. doi:10.2113/gsjfr.17.2.153
- D’Hondt, S.L., Jørgensen, B.B., Miller, D.J., et al., 2003. *Proc. ODP, Init. Repts.*, 201: College Station, TX (Ocean Drilling Program). doi:10.2973/odp.proc.ir.201.2003
- Droser, M.L., and Bottjer, D.J., 1986. A semiquantitative field classification of ichnofabric. *J. Sediment. Res.*, 56(4):558–559. <http://jsedres.sepmonline.org/cgi/content/abstract/56/4/558>
- Droser, M.L., and Bottjer, D.J., 1991. Trace fossils and ichnofabric in Leg 119 cores. In Barron, J., Larsen, B., et al., *Proc. ODP, Sci. Results*, 119: College Station, TX (Ocean Drilling Program), 635–641. doi:10.2973/odp.proc.sr.119.206.1991
- Ellis, D.V., 1986. Neutron porosity devices—what do they measure? *First Break*, 4(3):11–17. doi:10.3997/1365-2397.1986005
- Ellis, D.V., and Singer, J.M., 2007. *Well Logging for Earth Scientists*, (2nd ed.): Dordrecht, The Netherlands (Springer).
- Evans, M., Best, D., Hilenka, J., Kurkoski, P., and Sloan, W., 1995. Improved formation evaluation using azimuthal porosity data while drilling. *Proc.—SPE Annu. Tech. Conf.*, Pap. SPE 30546.
- Expedition 315 Scientists, 2009. Expedition 315 methods. In Kinoshita, M., Tobin, H., Ashi, J., Kimura, G., Lalle-mant, S., Scream, E.J., Curewitz, D., Masago, H., Moe, K.T., and the Expedition 314/315/316 Scientists, *Proc. IODP*, 314/315/316: Washington, DC (Integrated Ocean Drilling Program Management International, Inc.). doi:10.2204/iodp.proc.314315316.123.2009
- Expedition 316 Scientists, 2009. Expedition 316 methods. In Kinoshita, M., Tobin, H., Ashi, J., Kimura, G., Lalle-mant, S., Scream, E.J., Curewitz, D., Masago, H., Moe, K.T., and the Expedition 314/315/316 Scientists, *Proc. IODP*, 314/315/316: Washington, DC (Integrated Ocean Drilling Program Management International, Inc.). doi:10.2204/iodp.proc.314315316.132.2009
- Fisher, A.T., and Underwood, M.B., 1995. Calibration of an X-ray diffraction method to determine relative mineral abundances in bulk powders using matrix singular value decomposition: a test from the Barbados accretionary complex. In Shipley, T.H., Ogawa, Y., Blum, P., et al., *Proc. ODP, Init. Repts.*, 156: College Station, TX (Ocean Drilling Program), 29–37. doi:10.2973/odp.proc.ir.156.103.1995
- Fisher, R.V., and Schmincke, H.-U., 1984. *Pyroclastic Rocks*: New York (Springer-Verlag).
- Flemings, P.B., Behrmann, J.H., John, C.M., and the Expedition 308 Scientists, 2006. *Proc. IODP*, 308: College Station, TX (Integrated Ocean Drilling Program Management International, Inc.). doi:10.2204/iodp.proc.308.2006

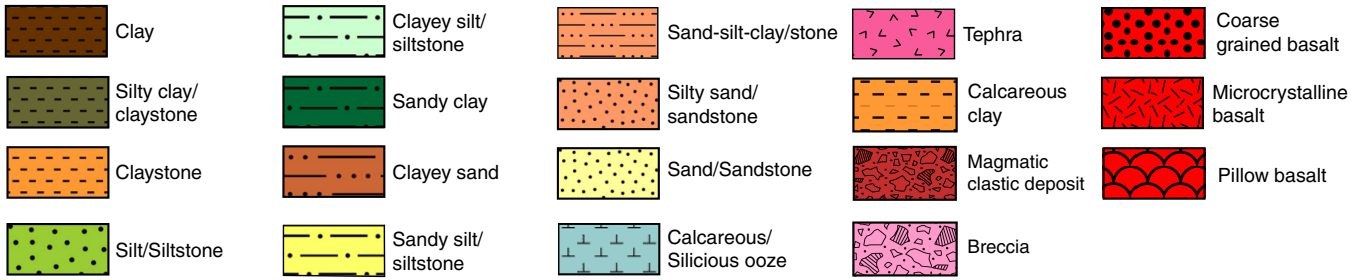
- Fuller, M., 1969. Magnetic orientation of borehole cores. *Geophysics*, 34(5):772–774. doi:10.1190/1.1440047
- Gieskes, J.M., Gamo, T., and Brumsack, H., 1991. Chemical methods for interstitial water analysis aboard *JOIDES Resolution*. *ODP Tech. Note*, 15. doi:10.2973/odp.tn.15.1991
- Graber, K.K., Pollard, E., Jonasson, B., and Schulte, E. (Eds.), 2002. Overview of Ocean Drilling Program engineering tools and hardware. *ODP Tech. Note*, 31. doi:10.2973/odp.tn.31.2002
- Gradstein, F.M., Ogg, J.G., and Smith, A. (Eds.), 2004. *A Geologic Time Scale 2004*: Cambridge (Cambridge Univ. Press). <http://cambridge.org/uk/catalogue/catalogue.asp?isbn=9780521781428>
- Harms, J.C., and Choquette, P.W., 1965. Geologic evaluation of a gamma-ray porosity device. *Trans. SPWLA Annu. Logging Symp.*: 6(2):C1–C37.
- Hay, W.W., 1970. Calcareous nannofossils from cores recovered on Leg 4. In Bader, R.G., Gerard, R.D., et al., *Init. Repts. DSDP*, 4: Washington, DC (U.S. Govt. Printing Office), 455–501. doi:10.2973/dsdp.proc.4.123.1970
- Heard, T.G., and Pickering, K.T., 2008. Trace fossils as diagnostic indicators of deep-marine environments, middle Eocene Ainsa-Jaca Basin, Spanish Pyrenees. *Sedimentology*, 55(4):809–844. doi:10.1111/j.1365-3091.2007.00922.x
- Heinz, P., Ruschmeier, W., and Hemleben, C., 2008. Live benthic foraminiferal assemblages at the Pacific continental margin of Costa Rica and Nicaragua. *J. Foraminiferal Res.*, 38(3):215–227. doi:10.2113/gsjfr.38.3.215
- Holtz, R.D., and Kovacs, W.D., 1981. *An Introduction to Geotechnical Engineering*: Englewood Cliffs, NJ (Prentice-Hall).
- House, C.H., Cragg, B.A., Teske, A., and the Leg 201 Scientific Party, 2003. Drilling contamination tests during ODP Leg 201 using chemical and particulate tracers. In D'Hondt, S.L., Jørgensen, B.B., Miller, D.J., et al., *Proc. ODP, Init. Repts.*, 201: College Station, TX (Ocean Drilling Program), 1–19. doi:10.2973/odp.proc.ir.201.102.2003
- Ingle, J.C., Jr., Keller, G., and Kolpack, R.L., 1980. Benthic foraminiferal biofacies, sediments and water masses of the southern Peru-Chile Trench area, southeastern Pacific Ocean. *Micropaleontology*, 26(2):113–150. doi:10.2307/1485435
- Jones, R.W., 1994. *The Challenger Foraminifera*: New York (Oxford).
- Keenan, J.H., Keyes, F.G., Hill, P.G., and Moore, J.G., 1978. *Steam Tables: Thermodynamic Properties of Water Including Vapor, Liquid, and Solid Phases (international system of units; S.I.)*: New York (John Wiley & Sons).
- Kennett, J.P., and Srinivasan, M.S., 1983. *Neogene Planktonic Foraminifera: A Phylogenetic Atlas*: Stroudsburg, PA (Hutchinson Ross).
- Kimura, G., Silver, E.A., Blum, P., et al., 1997. *Proc. ODP, Init. Repts.*, 170: College Station, TX (Ocean Drilling Program). doi:10.2973/odp.proc.ir.170.1997
- Kinoshita, M., Tobin, H., Ashi, J., Kimura, G., Lallemand, S., Scream, E.J., Curewitz, D., Masago, H., Moe, K.T., and the Expedition 314/315/316 Scientists, 2009. *Proc. IODP*, 314/315/316: Washington, DC (Integrated Ocean Drilling Program Management International, Inc.). doi:10.2204/iodp.proc.314315316.2009
- Kirschvink, J.L., 1980. The least-squares line and plane and the analysis of palaeomagnetic data. *Geophys. J. R. Astron. Soc.*, 62(3):699–718. doi:10.1111/j.1365-246X.1980.tb02601.x
- Kopf, A., Araki, E., Toczko, S., and the Expedition 332 Scientists, 2011. NanTroSEIZE Stage 2: riserless observatory. *IODP Prel. Rept.*, 332. doi:10.2204/iodp.pr.332.2011
- Kvenvolden, K.A., and McDonald, T.J., 1986. Organic geochemistry on the *JOIDES Resolution*—an assay. *ODP Tech. Note*, 6: College Station, TX (Ocean Drilling Program). doi:10.2973/odp.tn.6.1986
- Labat, C., Brady, S., Everett, M., Ellis, D., Doghmi, M., Tomlinson, J.C., and Shehab, G., 2002. 3D azimuthal LWD caliper *Proc.—SPE Annu. Tech. Conf.*, Pap. SPE 77526.
- Loeblich, A.R., Jr., and Tappan, H., 1988. *Foraminiferal Genera and Their Classification*: New York (Van Nostrand Reinhold).
- Manheim, F.T., and Sayles, F.L., 1974. Composition and origin of interstitial waters of marine sediments, based on deep sea drill cores. In Goldberg, E.D. (Ed.), *The Sea* (Vol. 5): *Marine Chemistry: The Sedimentary Cycle*: New York (Wiley), 527–568.
- Martini, E., 1971. Standard Tertiary and Quaternary calcareous nannoplankton zonation. *Proc. Int. Conf. Planktonic Microfossils*, 2:739–785.
- Mikada, H., Becker, K., Moore, J.C., Klaus, A., et al., 2002. *Proc. ODP, Init. Repts.*, 196: College Station, TX (Ocean Drilling Program). doi:10.2973/odp.proc.ir.196.2002
- Moore, J.C., Klaus, A., et al., 1998. *Proc. ODP, Init. Repts.*, 171A: College Station, TX (Ocean Drilling Program). doi:10.2973/odp.proc.ir.171A.1998
- Munsell Color Company, Inc., 2000. *Munsell Soil Color Chart*: New York (Gretag-Macbeth).
- Murray, R.W., Miller, D.J., and Kryc, K.A., 2000. Analysis of major and trace elements in rocks, sediments, and interstitial waters by inductively coupled plasma–atomic emission spectrometry (ICP-AES). *ODP Tech. Note*, 29. doi:10.2973/odp.tn.29.2000
- Okada, H., and Bukry, D., 1980. Supplementary modification and introduction of code numbers to the low-latitude coccolith biostratigraphic zonation (Bukry, 1973; 1975). *Mar. Micropaleontol.*, 5:321–325. doi:10.1016/0377-8398(80)90016-X
- Ogg, J.G., Ogg, G., and Gradstein, F.M., 2008. *The Concise Geologic Time Scale*: Cambridge (Cambridge Univ. Press). <http://www.cambridge.org/catalogue/catalogue.asp?isbn=9780521898492>
- Pimmel, A., and Claypool, G., 2001. Introduction to shipboard organic geochemistry on the *JOIDES Resolution*. *ODP Tech. Note*, 30. doi:10.2973/odp.tn.30.2001

- Pindell, J.L., Cande, S.C., Pitman, W.C., III, Rowley, D.B., Dewey, J.F., Labrecque, J., and Haxby, W., 1988. A plate-kinematic framework for models of Caribbean evolution. *Tectonophysics*, 155(1–4):121–138. doi:10.1016/0040-1951(88)90262-4
- Ratcliffe, E.H., 1960. The thermal conductivities of ocean sediments. *J. Geophys. Res.*, 65(5):1535–1541. doi:10.1029/JZ065i005p01535
- Richter, C., Acton, G., Endris, C., and Radsted, M., 2007. Handbook for shipboard paleomagnetists. *ODP Tech. Note*, 34. doi:10.2973/odp.tn.34.2007
- Richter, T.O., van der Gaast, S., Koster, B., Vaars, A., Gieles, R., de Stigter, H.C., De Haas, H., and van Weering, T.C.E., 2006. The Avaatech XRF Core Scanner: technical description and applications to NE Atlantic sediments. In Rothwell, R.G. (Ed.), *New Techniques in Sediment Core Analysis*. Geol. Soc. Spec. Publ., 267(1):39–50. doi:10.1144/GSL.SP.2006.267.01.03
- Riedel, M., Collett, T., Malone, M.J., and IODP Expedition 311 Scientists, 2009. Gas hydrate drilling transect across northern Cascadia margin—IODP Expedition 311. *Geol. Soc. Spec. Publ.*, 319:11–19. doi:10.1144/SP319.2
- Rothwell, R.G., 1989. *Minerals and Mineraloids in Marine Sediments: An Optical Identification Guide*: London (Elsevier).
- Saffer, D., McNeill, L., Byrne, T., Araki, E., Toczko, S., Eguichi, N., Takahashi, K., and the Expedition 319 Scientists, 2010. *Proc. IODP*, 319: Tokyo (Integrated Ocean Drilling Program management International, Inc.). doi:10.2204/iodp.proc.319.2010
- Shipley, T.H., Ogawa, Y., Blum, P., et al., 1995. *Proc. ODP, Init. Repts.*, 156: College Station, TX (Ocean Drilling Program). doi:10.2973/odp.proc.ir.156.1995
- Smith, D.C., Spivack, A.J., Fisk, M.R., Haveman, S.A., and Staudigel, H., 2000a. Tracer-based estimates of drilling-induced microbial contamination of deep sea crust. *Geomicrobiol. J.*, 17(3):207–219. doi:10.1080/01490450050121170
- Smith, D.C., Spivack, A.J., Fisk, M.R., Haveman, S.A., Staudigel, H., and the Leg 185 Shipboard Scientific Party, 2000b. Methods for quantifying potential microbial contamination during deep ocean coring. *ODP Tech. Note*, 28. doi:10.2973/odp.tn.28.2000
- Smith, P.B., 1963. Quantitative and qualitative analysis of the family *Boliviniidae*. *U.S. Geol. Surv. Prof. Pap.*, 429-A.
- Smith, P.B., 1964. Ecology of benthonic species. *U.S. Geol. Surv. Prof. Pap.* 429-B.
- Tauxe, L., Tucker, P., Petersen, N.P., and Labrecque, J.L., 1983. The magnetostratigraphy of Leg 73 sediments. *Palaeogeogr., Palaeoclimatol., Palaeoecol.*, 42(1–2):65–90. doi:10.1016/0031-0182(83)90039-1
- Vacquier, V., 1985. The measurement of thermal conductivity of solids with a transient linear heat source on the plane surface of a poorly conducting body. *Earth Planet. Sci. Lett.*, 74(2–3):275–279. doi:10.1016/0012-821X(85)90027-5
- van der Plas, L., and Tobi, A.C., 1965. A chart for judging the reliability of point counting results. *Am. J. Sci.*, 263(1):87–90. doi:10.2475/ajs.263.1.87
- Von Herzen, R., and Maxwell, A.E., 1959. The measurement of thermal conductivity of deep-sea sediments by a needle-probe method. *J. Geophys. Res.*, 64(10):1557–1563. doi:10.1029/JZ064i010p01557
- Wade, B.S., Pearson, P.N., Berggren, W.A., and Pälike, H., 2011. Review and revision of Cenozoic tropical planktonic foraminiferal biostratigraphy and calibration to the geomagnetic polarity and astronomical time scale. *Earth-Sci. Rev.*, 104(1–3):111–142. doi:10.1016/j.earsci-rev.2010.09.003
- Wentworth, C.K., 1922. A scale of grade and class terms for clastic sediments. *J. Geol.*, 30(5):377–392. doi:10.1086/622910
- Zijderveld, J.D.A., 1967. AC demagnetization of rocks: analysis of results. In Collinson, D.W., Creer, K.M., and Runcorn, S.K. (Eds.), *Methods in Palaeomagnetism*: New York (Elsevier), 254–286.
- Zoth, G., and Haenel, R., 1988. Appendix: 1. In Haenel, R., Rybach, L., and Stegena, L. (Eds.), *Handbook of Terrestrial Heat-Flow Density Determination: with Guidelines and Recommendations of the International Heat Flow Commission*: Dordrecht (Kluwer Acad. Publ.), 449–4668.

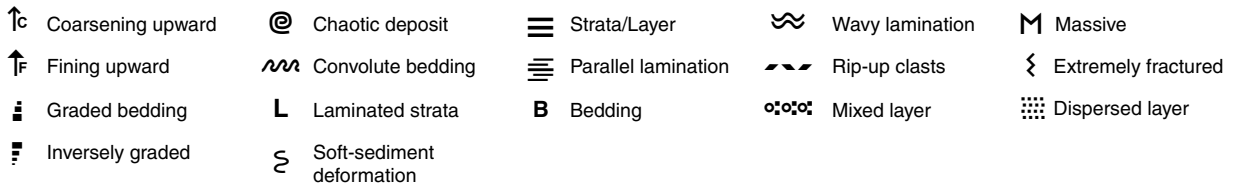
Publication: 12 April 2012
MS 334-102

Figure F1. Graphic patterns for sedimentary lithologies encountered during Expedition 334.

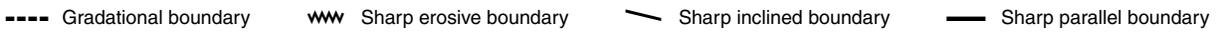
Lithology



Sedimentary structures



Boundary



Lithologic accessories



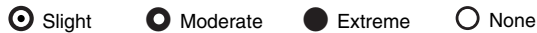
Shipboard samples



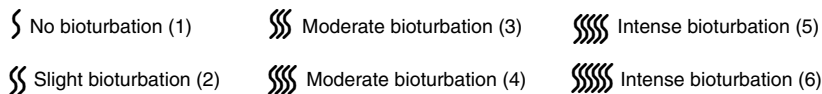
Fossils



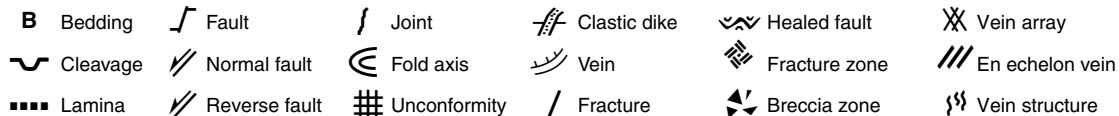
Drilling disturbance



Bioturbation



Measured structures



Dip

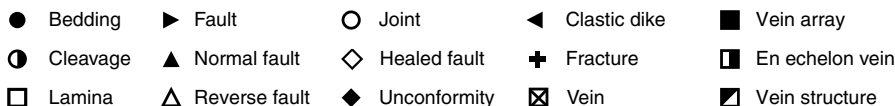


Figure F2. Diffractograms of mixtures of standard minerals showing positions of diagnostic XRD peaks used to calculate relative mineral abundances. Cl = total clay minerals, Q = quartz, P = plagioclase, Cc = calcite.

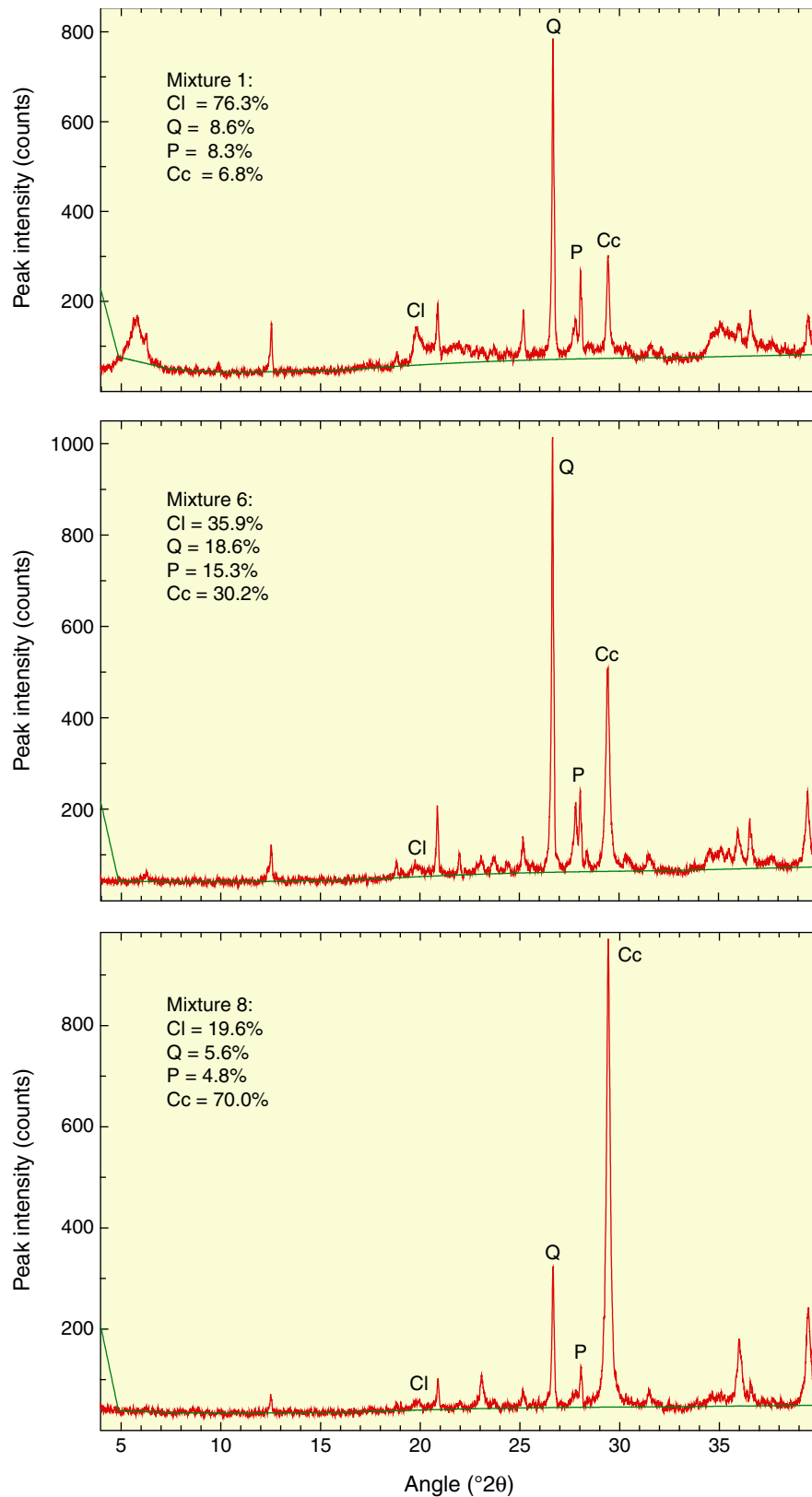
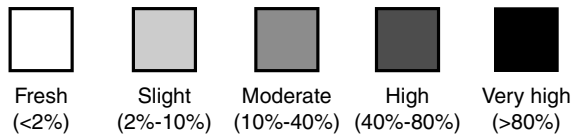


Figure F3. Graphic patterns for basement lithologies encountered during Expedition 334.

Alteration



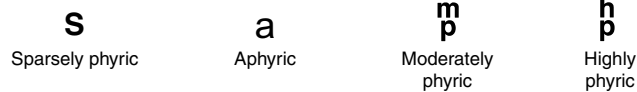
Shipboard samples

IC Inorganic carbon	PAL Paleontology	IW Interstitial water	XRD X-ray diffraction
HS Heaspace gas	PMAG Paleomagnetism	SS Smear slide	

Igneous features



Phenocryst abundance



Phenocryst type

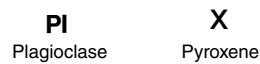




Figure F4. Example of log sheet used to record structural and orientation data and observations from working half of split core, Expedition 334.

Exp. 334 Structural Geology Observation Sheet

Site: _____

Core	Sec.	Structure ID	Top of struct	Bottom of struct	Core face app. plunge		2nd app. plunge		Striation on surface		Coherent int for pmag		P-mag pole		Note	
					az	plunge	az	plunge	rake	from	top	bottom	Dec	Inc		

Figure F5. Photograph of modified protractor used to measure apparent dips, trends, plunges, and rakes on planar and linear features in a split core, Expedition 334.

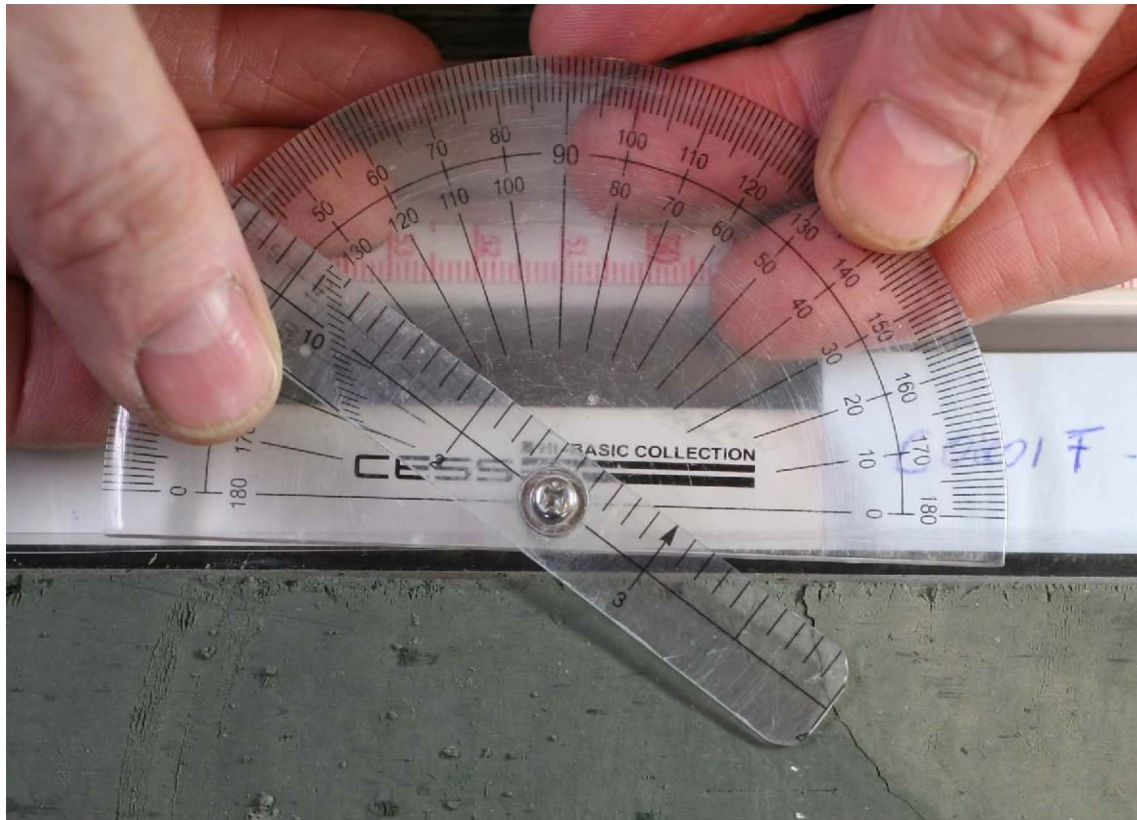


Figure F6. Diagram of core reference frame and x -, y -, z -coordinates used in orientation data calculations, Expedition 334.

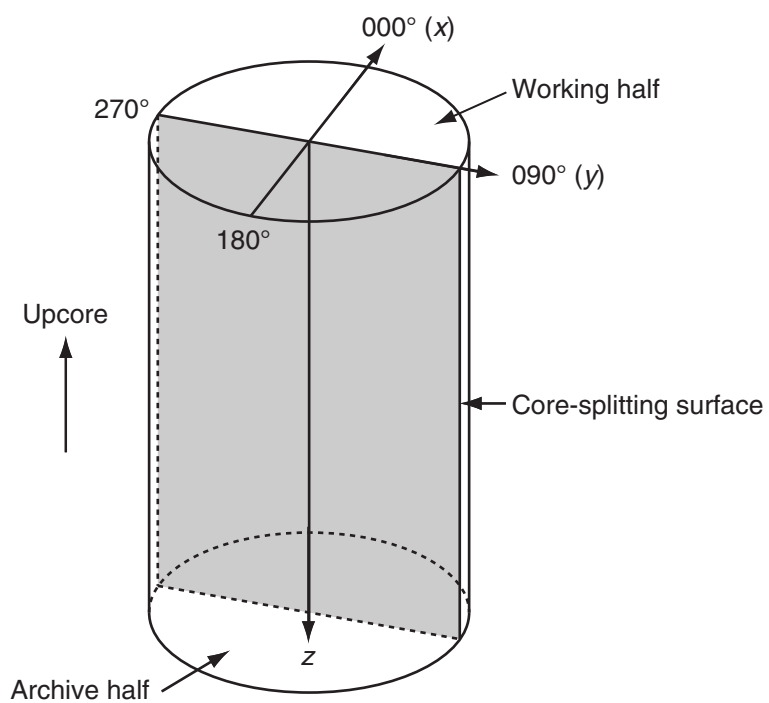


Figure F7. Lower hemisphere equal area projection showing the structural procedure for converting measured data to 3-D data, Expedition 334. **A.** Plane attitude determined using two apparent dips on two surfaces. Striation on the plane is also plotted. **B.** Restoration to the geographic coordinate using paleomagnetic data.

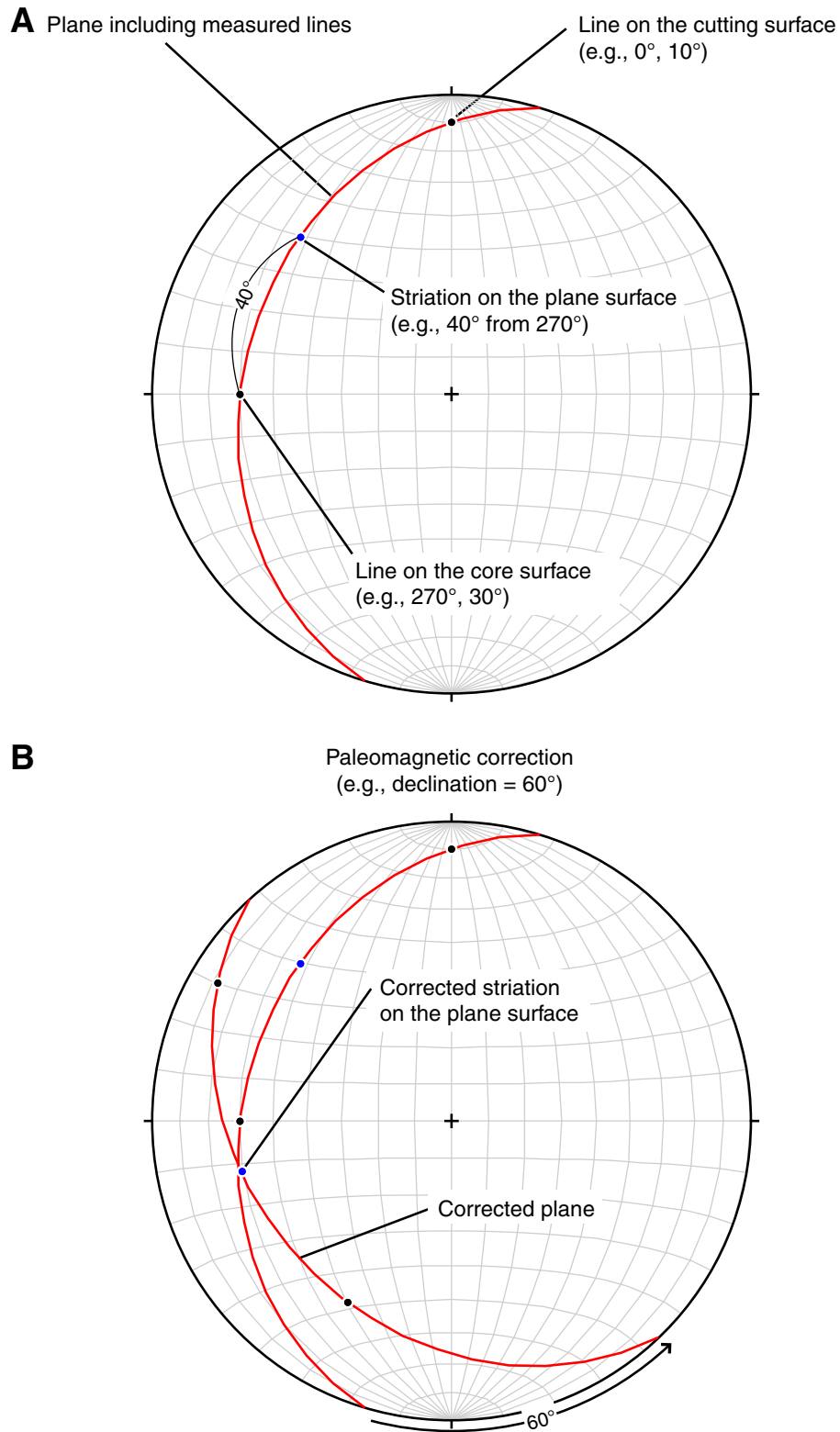


Figure F8. Diagram showing calculation of plane orientation (shaded) from two apparent dips. Intersections of split core surface, section perpendicular to split core surface, and section parallel to core direction with plane of interest are shown. (α_1, β_1) and (α_2, β_2) = azimuths and dips of traces of the plane on two sections, v_1 and v_2 = unit vectors parallel to traces of the plane on two sections, v_n = unit vector normal to plane.

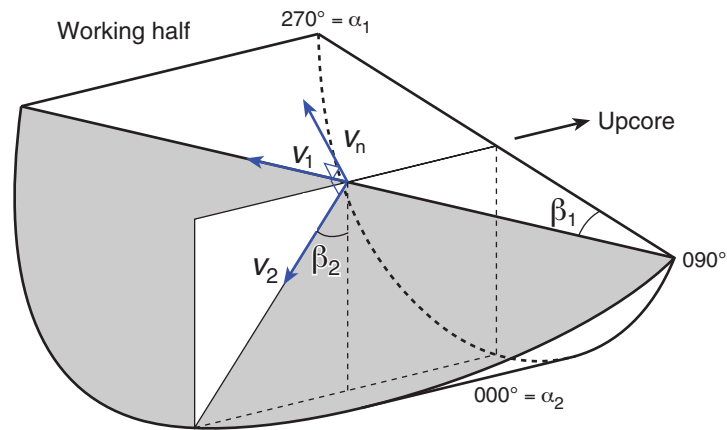


Figure F9. Diagrams of dip direction (α_d), right-hand rule strike (α_s), and dip (β) of a plane deduced from its normal azimuth (α_n) and dip (β_n). v_n = unit vector normal to plane. **A.** $\beta_n < 0^\circ$. **B.** $\beta_n \geq 0^\circ$.

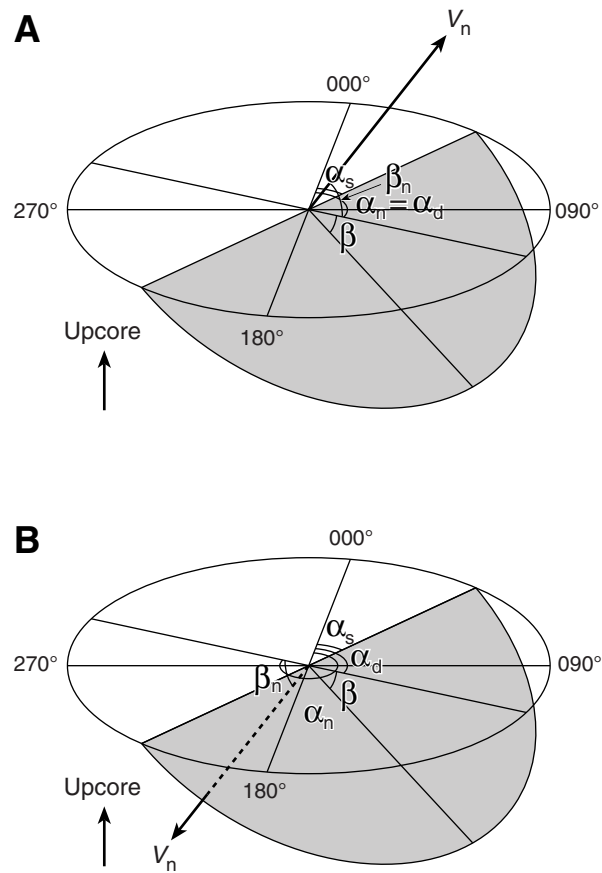


Figure F10. Diagram of apparent rake measurement of striations on a fault surface from 270° direction of split core surface trace. ϕ_a = apparent rake, v_n = unit vector normal to fault plane, v_c = unit vector normal to split core surface, v_i = unit vector parallel to the intersection line between fault plane and split core surface.

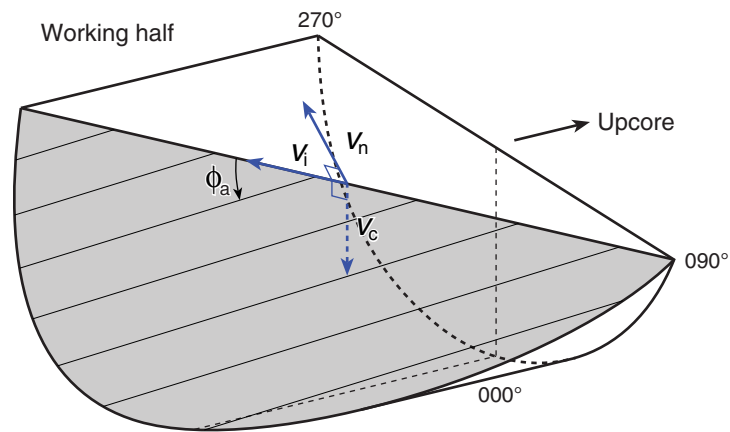


Figure F11. Diagrams of rake of striations (ϕ) deduced from the rake of intersection line between fault plane and split core surface (ϕ_i) and apparent rake measured (ϕ_a). α_s = right-hand rule strike of fault plane, v_n = unit vector normal to fault plane, v_c = unit vector normal to split core surface, v_i = unit vector parallel to intersection line between fault plane and split core surface. **A.** ϕ_a from top or 90° direction when fault plane dips westward. **B.** ϕ_a from bottom or 90° direction when fault plane dips eastward. **C.** ϕ_a from top or 270° direction when fault plane dips eastward. **D.** ϕ_a from bottom or 270° direction when fault plane dips westward.

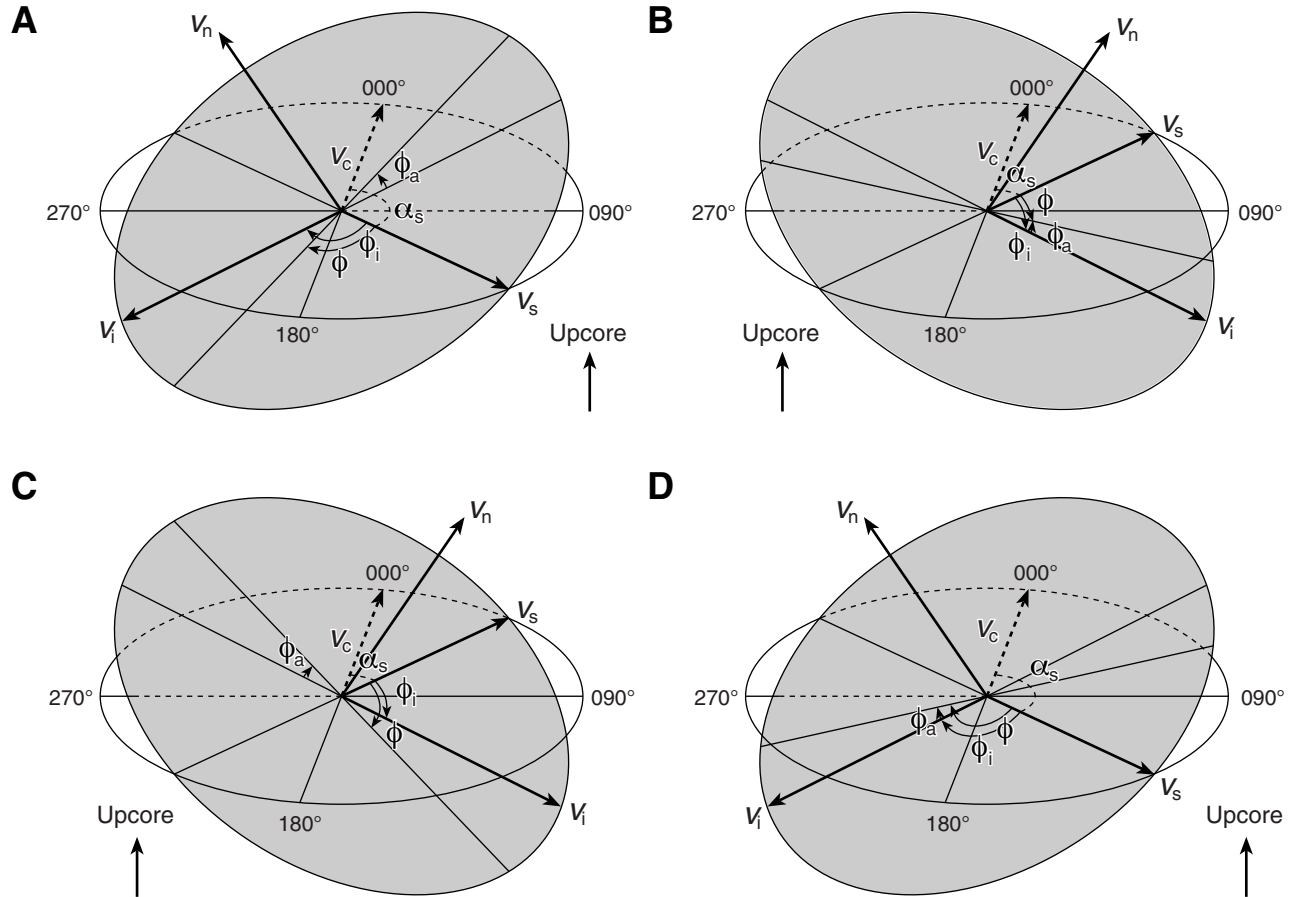


Figure F12. Diagrams of azimuth correction based on paleomagnetic data. α_p = paleomagnetic declination, α_d and α_s = dip direction and right-hand rule strike of a plane. **A.** Paleomagnetic inclination $\beta_p \geq 0^\circ$. **B.** $\beta_p < 0^\circ$.

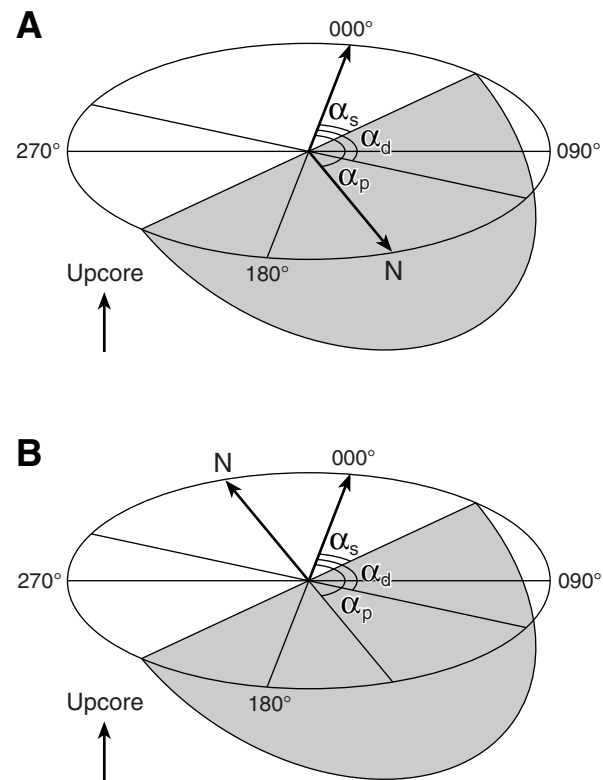




Figure F13. Schematic diagram of strategy used during Expedition 334 to collect an integrated sample set for geomicrobiology, which included interstitial water sampling, sediment characterization (cluster sample), headspace, and microbiology samples. WR = whole round.

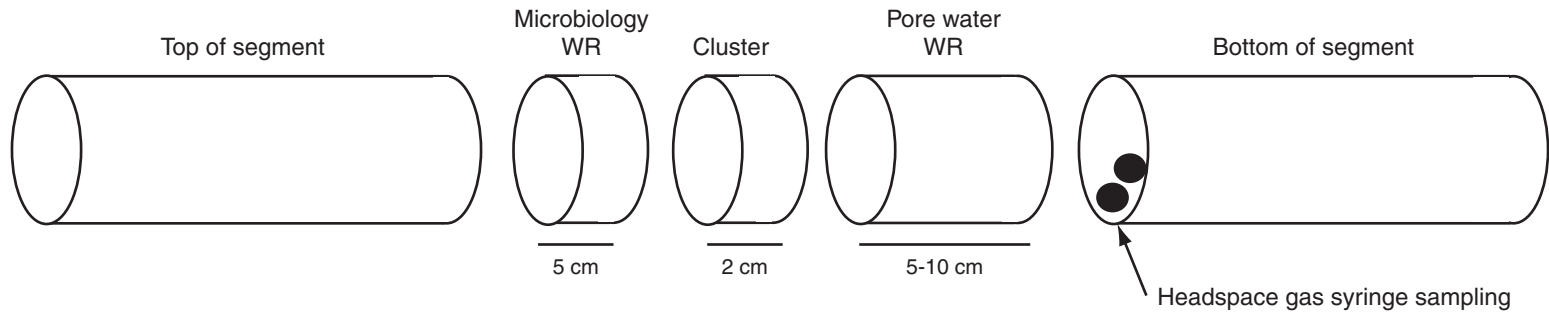


Figure F14. Diagram of superconducting rock magnetometer (SRM) coordinates onboard the *JOIDES Resolution* and for reported data (after Richter et al., 2007).

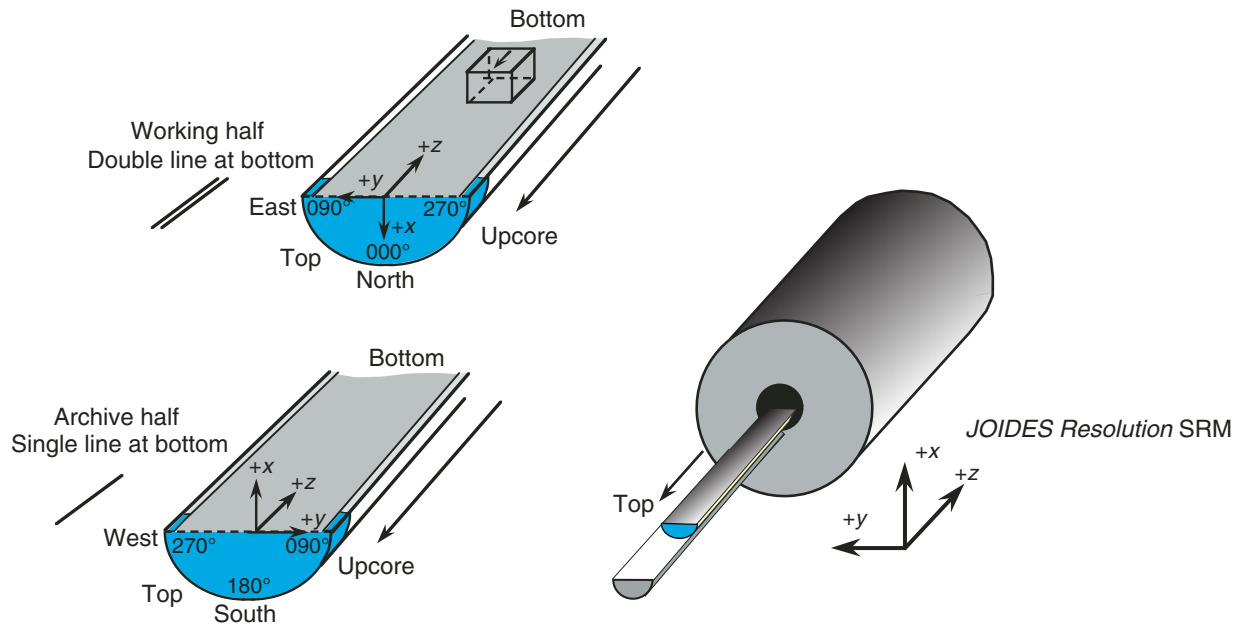


Figure F15. Plot of results from a comparative test of the *JOIDES Resolution's* superconducting rock magnetometer (SRM) filters using a sample core section of concrete materials. The concrete in the sample core section starts after an interval of ~ 0.38 m (unshaded region). The interval without sample near the sample end (~ 0.38 m) revealed strong signal because the sensor coils of the SRM have a ~ 20 cm corresponsive region.

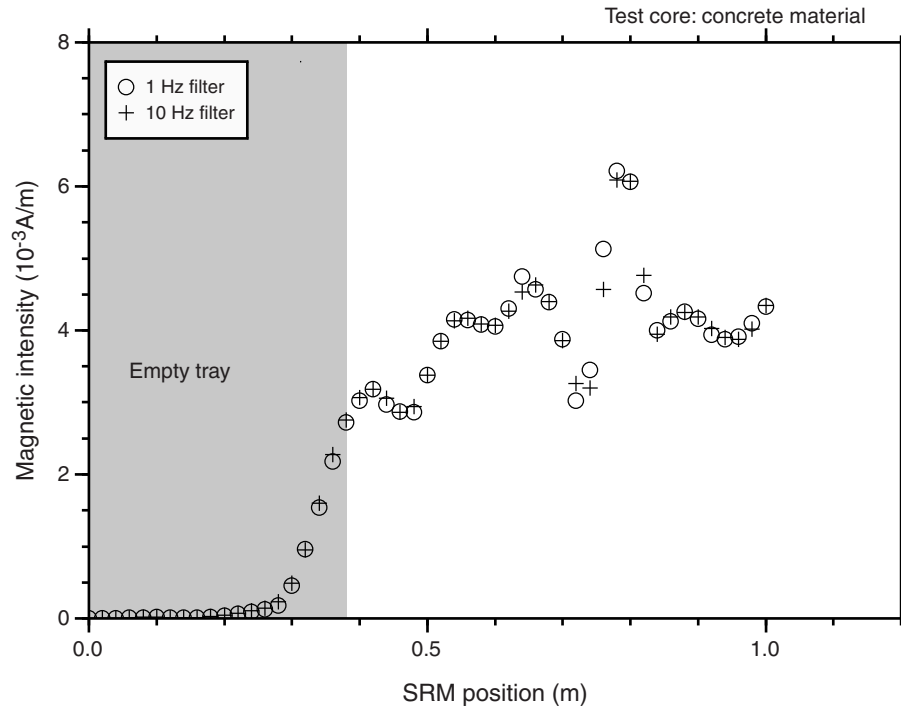


Figure F16. Diagram of LWD bottom-hole assembly used during Expedition 334. MWD = measurement while drilling.

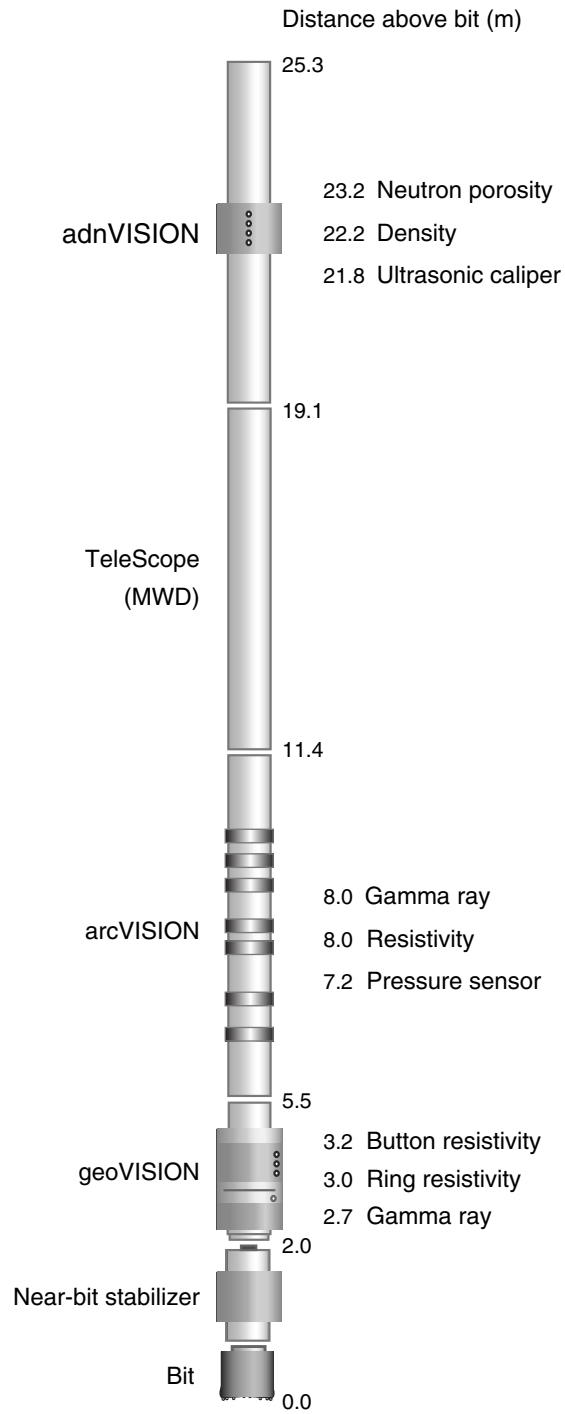


Figure F17. Unwrapped image of a vertical cylindrical borehole with horizontal planes as horizontal lines and dipping planes as sinusoidal curves. Modified after Bonner et al. (1996).

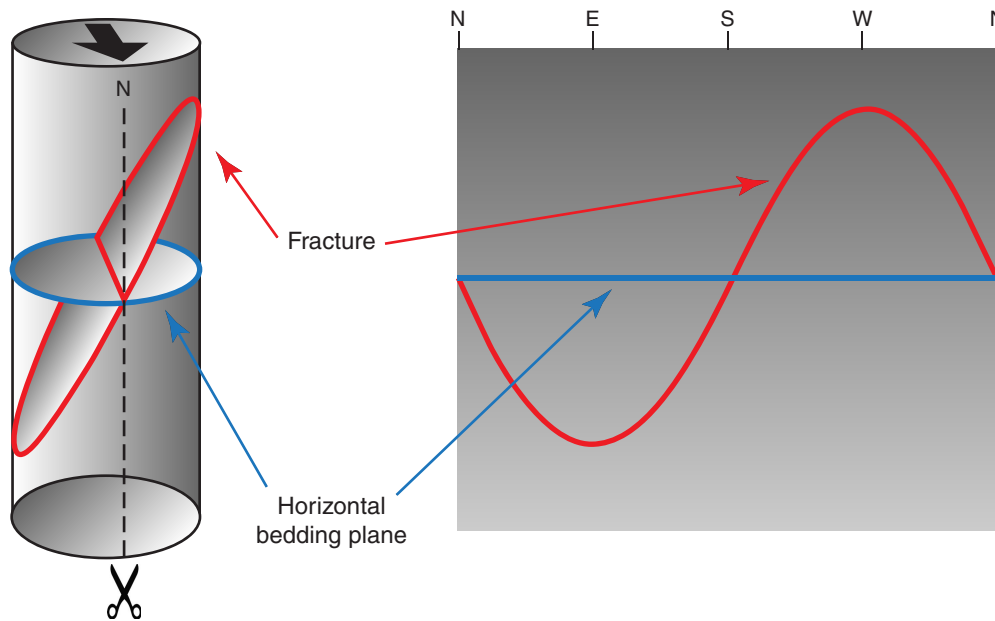


Table T1. Classification of volcanic lithologies, Expedition 334.

Size	Mixture		
	Tephra	Tuffite	Epiclastic deposit
>64 mm	Pyroclastic breccia	Tuffaceous breccia/conglomerate	Breccia/Conglomerate
2–64 mm	Lapillistone/Lapilli tuff	Tuffaceous gravel	Gravel
64 μm –2 mm	Coarse ash tuff	Tuffaceous sandstone	Sandstone
2–64 μm	Fine ash tuff	Tuffaceous siltstone	Siltstone
<2 μm	Volcanic dust	Tuffaceous volcanic dust	Claystone
Amount of pyroclasts (%):	≥ 75	<75 to >25	≤ 25

Modified classification scheme after Fisher and Schmincke (1984).

Table T2. Characteristic X-ray diffraction peaks for semiquantitative area analysis, Expedition 334.

Mineral	Reflection	d-value (\AA)	Peak position ($^{\circ}2\theta$)
Composite clay	Multiple	4.478	19.4–20.4
Quartz	101	3.342	26.3–27.0
Plagioclase	002	3.192	27.4–28.2
Calcite	104	3.035	29.1–29.7

Table T3. Normalization factors for calculation of relative mineral abundance using bulk powder X-ray diffraction analysis, Expedition 334.

Affected mineral in standard mixture	Normalization factors			
	Total clay	Quartz	Plagioclase	Calcite
Influencing mineral:				
Total clay	9.8956702E-03	-1.5889532E-04	-2.8855808E-04	-7.3842803E-04
Quartz	-4.7221169E-05	5.8782392E-04	-4.7869325E-05	-3.1098843E-05
Plagioclase	7.2794763E-04	-4.2840613E-05	1.3719777E-03	-3.6005495E-05
Calcite	4.2042411E-05	3.3021188E-06	-4.1329499E-06	1.3071455E-03

Singular value decomposition was used to compute factors, following Fisher and Underwood (1995).

**Table T4.** Subsampling protocol for shipboard and shore-based samples collected during Expedition 334.

	O/H	DOC	DIC	Halogens	VFA	Fe/Mo*	REE	B isotopes	⁷ Li/ ⁶ Li ⁸⁷ Sr/ ⁸⁶ Sr	Noble gas isotopes	Shipboard			Total
Subsample container:	2 mL screw top	1.5 mL screw top	2 mL Agilent vials	2 mL screw top	Glass vials	Nalgene 8 mL bottle	Nalgene 8 mL bottle	4 mL HDPE bottle	4 mL Nalgene acidified to pH 2	2 mL Cu tubing	5 mL tube	4 mL HDPE bottle	4 mL HDPE bottle	
Treatment:		Frozen	HgCl ₂ 10 µL		Freeze at -20°C	HNO ₃	HNO ₃		HNO ₃	Room temperature		HNO ₃	ZnAc	
>55 mL	2	1	2	2	3	10	8	2	3	2	6	4	7	52
50 mL	2	1	2	2	3	10	6	2	3	2	6	4	7	50
45 mL	2	1	2	2	2	8	5	2	3	2	6	4	6	45
40 mL	2	1	2	2	2	8		2	3	2	6	4	6	40
35 mL	2	1	2	2	2		5	2	3	2	6	4	4	35
30 mL	2	1	1	2	2	5		2	3	2	4	4	2	30
25 mL	2	1	1	2	2			2	3	2	4	4	2	25
20 mL	1	1	1	1	2				2	2	4	4	2	20
20 mL	1	1	1	1				2	2	2	4	4	2	20
15 mL	1			1		0	0	2		2	4	4	1	15
15 mL	1	1	1	1	2		0	0	3	0	1	3	2	15
10 mL	1		1					2	2	0	1	2	1	10
10 mL				1						2	4	2	1	10
5 mL	1			1							0.1	2	1	5.1
5 mL	1								1		0.1	2	1	5.1
2 mL	1										0.1	1		2.1
1 mL	1										0.1			1.1

* = Fe/Mo only to one core below sulfate–methane transition zone. Duplicate entries for a given volume (designated in bold) reflect alternate samples. DOC = dissolved organic carbon, DIC = dissolved inorganic carbon, VFA = volatile fatty acids, REE = rare-earth element. HDPE = high-density polyethylene.

Table T5. Division of cluster samples, Expedition 334.

Sample type	Volume (cm ³)
10 cm cluster sample:	
Shipboard XRD	50
Shipboard physical properties	50
Shore-based Fe/Mo (MF)	50
Shore-based biomarkers (MN)	50
Shore-based chemistry (ES)	50
Shore-based CEC (MC)	50
2 cm cluster sample:	
Shipboard XRD	5
Shipboard physical properties	10
Shore-based Fe/Mo (MF)	5
Shore-based biomarkers (MN)	20
Shore-based chemistry (ES)	20
Shore-based CEC (MC)	20

XRD = X-ray diffraction, CEC = cation exchange capacity. MF = Michael Formolo, MN = Marianne Nuzzo, ES = Evan Solomon, MC = Marianne Conin.

Table T6. Ages used for magnetostratigraphy, Expedition 334 (data from Gradstein et al., 2004). (Continued on next page.)

Interval age (Ma)		Chron/Subchron
Top	Bottom	
0.000	0.781	C1n
0.988	1.072	C1r.1n
1.173	1.185	C1r.2n
1.778	1.945	C2n
2.581	3.032	C2An.1n
3.116	3.207	C2An.2n
3.330	3.596	C2An.3n
4.187	4.300	C3n.1n
4.493	4.631	C3n.2n
4.799	4.896	C3n.3n
4.997	5.235	C3n.4n
6.033	6.252	C3An.1n
6.436	6.733	C3An.2n
7.140	7.212	C3Bn
7.251	7.285	C3Br.1n
7.454	7.489	C3Br.2n
7.528	7.642	C4n.1n
7.695	8.108	C4n.2n
8.254	8.300	C4r.1n
8.769	9.098	C4An
9.321	9.409	C4Ar.1n
9.656	9.717	C4Ar.2n
9.779	9.934	C5n.1n
9.987	11.040	C5n.2n
11.118	11.154	C5r.1n
11.554	11.614	C5r.2n
12.041	12.116	C5An.1n
12.207	12.415	C5An.2n
12.730	12.765	C5Ar.1n
12.820	12.878	C5Ar.2n
13.015	13.183	C5AAn
13.252	13.466	C5ABn
13.734	14.095	C5ACn
14.194	14.581	C5ADn
14.784	14.877	C5Bn.1n
15.032	15.160	C5Bn.2n
15.974	16.268	C5Cn.1n
16.303	16.472	C5Cn.2n
16.543	16.721	C5Cn.3n
17.235	17.533	C5Dn
18.056	18.524	C5En
18.748	19.722	C6n
20.040	20.213	C6An.1n
20.439	20.709	C6An.2n
21.083	21.159	C6AAn
21.659	21.688	C6AAr.2n
21.767	21.936	C6Bn.1n
21.992	22.268	C6Bn.2n
22.564	22.758	C6Cn.1n
22.902	23.030	C6Cn.2n
23.249	23.375	C6Cn.3n
24.044	24.102	C7n.1n
24.146	24.556	C7n.2n
24.915	25.091	C7An
25.295	25.444	C8n.1n
25.492	26.154	C8n.2n
26.714	27.826	C9n
28.186	28.450	C10n.1n
28.525	28.715	C10n.2n
29.451	29.740	C11n.1n
29.853	30.217	C11n.2n
30.627	31.116	C12n
33.266	33.738	C13n
34.782	35.043	C15n
35.404	35.567	C16n.1n
35.707	36.276	C16n.2n
36.512	37.235	C17n.1n

Table T6 (continued).

Interval age (Ma)		Chron/Subchron
Top	Bottom	
37.345	37.549	C17n.2n
37.610	37.771	C17n.3n
38.032	38.975	C18n.1n
39.041	39.464	C18n.2n
40.439	40.671	C19n
41.590	42.774	C20n
45.346	47.235	C21n
48.599	49.427	C22n
50.730	50.932	C23n.1n
51.057	51.901	C23n.2n
52.648	53.004	C24n.1n
53.116	53.167	C24n.2n
53.286	53.808	C24n.3n
56.665	57.180	C25n
58.379	58.737	C26n
61.650	61.983	C27n
63.104	64.128	C28n
64.432	65.118	C29n

Table T7. Measurement acronyms and units, vertical resolutions, and depths of investigation (where available) of wireline tools, Expedition 334.

Tool	Output	Explanation	Unit	Vertical resolution (cm)	Depth of investigation (cm)
adnVISION 675	CLXX	Azimuthal Density Neutron Tool Ultrasonic caliper along axes XX, where XX = 15, 26, 37, 48 (for axes 1 and 5, 2 and 6, etc.)	inch		
	DCAV	Average density caliper	inch		
	TNPH	Thermal neutron porosity	%	31	
	PEF	Photoelectric factor	b/e ⁻		
	RHOB	Density	g/cm ³	15	
	IDRO	Image-derived density	g/cm ³		
			Oriented density images of borehole wall Oriented images of borehole radius from density caliper		
arcVISION 675	AXXH, AXXL, AXXB	Array Resistivity Compensated Tool Attenuation resistivity at source-receiver spacing XX, where XX = 16, 22, 28, 34, and 40 inches	Ωm	55–122	48–102
	PXXH, PXXL, PXXB	Phase-shift resistivity at source-receiver spacing XX, where XX = 16, 22, 28, 34, and 40 inches	Ωm	21–30	33–79
		In the output acronyms above, H = 2 MHz resistivity, L = 400 kHz resistivity, and B = blended resistivity			
	GR_ARC	Calibrated gamma ray	gAPI	46	
	APRS_ARC	Downhole annulus pressure	psi		
	ATMP	Downhole annulus temperature	°C		
geoVISION 675	GR_CAL	Resistivity at the Bit Tool Calibrated gamma ray	gAPI	46	
	RES_BIT	Bit resistivity	Ωm	30–61	30
	RES_RING	Ring resistivity	Ωm	5–8	18
	RES_BD	Deep button resistivity average	Ωm	5–8	13
	RES_BM	Medium button resistivity average	Ωm	5–8	8
	RES_BS	Shallow button resistivity average	Ωm	5–8	2.5
			Oriented resistivity images of the borehole wall Oriented gamma ray images of the borehole wall		